Attenuation Tomography Beneath the Rocky Mountain Front: Implications for the Physical State of the Upper Mantle

Oliver S. Boyd and Anne F. Sheehan

Dept. of Geological Sciences and CIRES, University of Colorado, Boulder, CO 80309

Utilizing the Rocky Mountain Front (RMF) broadband seismic dataset acquired in 1992, this study has derived the seismic attenuation structure underlying part of the Southern Rocky Mountains and surrounding areas through measurements of differential t^* of S-phase waveforms. Previous studies of the area include P, S and surface wave travel time tomography and all indicate slow upper mantle velocities below the Rocky Mountain region. Calculations of intrinsic attenuation coupled with current velocity models aid in the determination of temperature, partial melt distributions, and compositional variation. A N-S zone of high shear wave attenuation ($Q_s \approx 30$) is found in the mantle beneath the Rocky Mountains and lies east of the region of lowest shear wave velocity. Relationships between shear wave attenuation and shear wave velocity are consistent with both thermal and compositional variability. Along the eastern Colorado Rockies and due north of the Rio Grande Rift, the relationships are consistent with an interpretation of elevated temperatures, up to 50 K at 125 km depth. West of this region low velocities and low attenuation suggest either unusual composition or very high temperatures. The low density mantle material beneath the Colorado Rocky Mountains in addition to increased crustal thickness and low density crustal intrusions provides a density contrast sufficient to support its overburden.

1. INTRODUCTION

For decades, geologists have questioned the mechanisms responsible for the high topography of the Rocky Mountains. Are the mountains supported by crustal thickening due to shortening (Airy root) or are there lateral density contrasts in the crust (Pratt compensation)? Is the lithosphere sufficiently rigid to support the topography? Does support come from the mantle rather than the crust? Measurements of crustal thickness by Sheehan et al. [1995] and Li et al. [2002] indicate an increase in crustal thickness that is not entirely able to support the overlying Rocky Mountains. Models of flexural support indicate that little of the observed topography is supported by bending of the elastic plate [*Sheehan et al.*, 1995]. These observations imply that regions of the crust and/or mantle have a reduced relative density.

Previous measurements that have explored the role of reduced crust/mantle density centered on measuring the change in seismic velocity across the region. Lee and Grand [1996], using the Rocky Mountain Front seismic dataset, measured shear wave travel times from teleseismic S-phase arrivals beneath the Colorado Rocky Mountains. The resulting shear wave velocity structures indicate reduced upper mantle velocity directly beneath the Colorado Rocky Mountains (Figure 1). The reduced upper mantle velocities trend north-south beneath the Colorado Rocky Mountains where the minimum shear wave velocity, -9% relative to western Kansas, occurs along this trend northwest of the Rio Grande Rift. Hessler [1997] produced a similar map from P wave travel time tomography but with smaller variations in P wave velocity, -4% (also summarized by Lerner-Lam et al. [1998]). Li et al. [2002] measured surface wave dispersion and inverted for crustal and upper mantle shear wave velocity. The greatest difference between the models of Lee and Grand and Li et al. is from 50 to 100 km depth beneath southwest Colorado where Lee and Grand's greatest decrease in shear velocity, -9%, corresponds to a decrease of only 6% from the model of Li et al. In addition, this position correlates with Li et al.'s thickest crust. Li et al. also find slow crustal shear velocities beneath the Sawatch Range in central Colorado which is correlated with high heat flow [*Decker et al.*, 1988]. Decker et al. used heat flow measurements and Bouguer gravity anomalies to infer the presence of granitic intrusions that were emplaced in the Miocene through the Quaternary. Li et al. point out that this

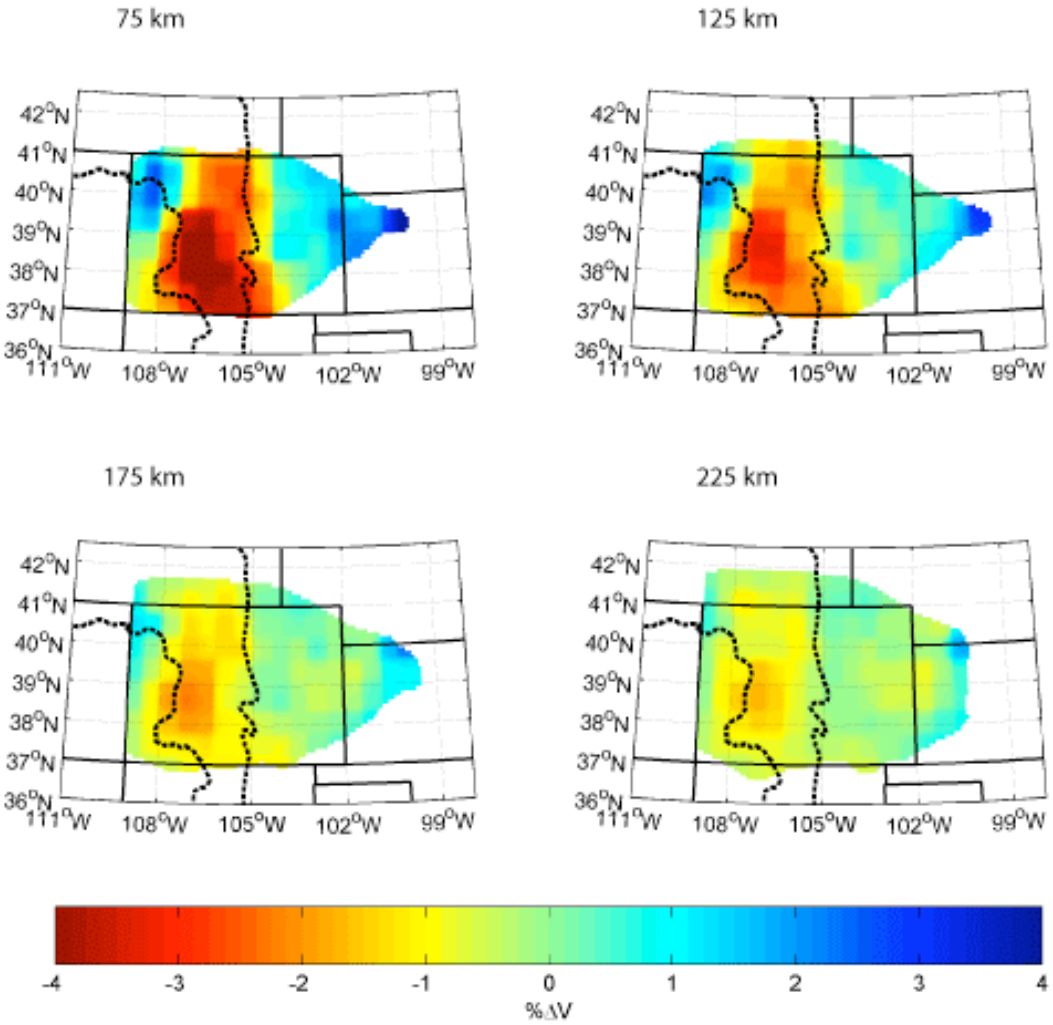

Figure 1. Horizontal slices of shear velocity variation [Lee and Grand, 1996] at four depths. Solid black lines denote state boundaries. Thick dashed solid lines delineate the Rocky Mountain region. Negative values (white) indicate slower velocities. Shear velocities beneath the Colorado Rocky Mountains are reduced by up to 9% relative to western Kansas. The transition to higher velocities in the east is believed to signify the transition to the stable craton.

compositional variation could explain the reduced shear velocities.

Changes to seismic velocity can result from changes to several material properties including temperature, composition and partial melt. If Lee and Grand's measured 9% lateral decrease in shear velocity in the upper mantle were due solely to increased temperature, using the scaling relations of Nataf and Ricard [1996] for changes in velocity with respect to temperature,

$$\frac{\partial \ln V_S}{\partial T} = -1.1 \times 10^{-4} K^{-1}, \qquad (1)$$

changes in temperature would be over 800 K. Lateral changes of this magnitude are unlikely. Such changes would produce density contrasts far exceeding those required to support the Rocky Mountains as well as produce wide spread melting.

Karato [1993] shows that velocity-temperature scaling relationships are dependent on attenuation (Q^{-1}), a fact that Nataf and Ricard briefly considered but did not fully exploit. Using Karato's relations with a Q of 50, a 9% S-wave velocity contrast will predict a change in temperature of almost 400 K. If only half of the measured velocity contrast is attributable to changes in temperature, a Q of 50 coupled with ΔV_S of 4.5% implies a change in temperature of only 200 K.

Attenuation models coupled with velocity models can also lead to models of the unrelaxed velocity [*Minster and Anderson*, 1981] which is sensitive to composition including the effects of partial melt [*Duffy and Anderson*, 1989; *Hammond and Humphreys*, 2000b]. If half of the measured velocity contrast were due to partial melt, Hammond and Humphreys [2000b] predicts that a 5% decrease in shear velocity would accompany a 0.6% increase in partial melt.

Previous studies of the attenuation structure beneath western North America indicate broad regional variations. Lay and Wallace [1988] examined multiple ScS wave attenuation west of the Rocky Mountains and found the highest attenuation values, $Q_{ScS} = 95 \pm 4$, beneath the Basin and Range. The lowest attenuation values, $Q_{ScS} = 344 \pm 88$, were measured beneath the Pacific Northwest. Al-Khatib and Mitchell [1991] measured Rayleigh wave attenuation coefficients across several regions of western North America. One measurement traversed the eastern Colorado Rocky Mountains on its way from southern New Mexico to Edmonton, Alberta. Average Q_β along this path reaches a minimum of 35 at 150 km depth. A higher resolution study [*Slack et al.*, 1996] measured P and S wave travel time delays and differential t^* across the Rio Grande Rift. Differential t^* spans a range of 3 seconds for S-waves and 2 seconds for P-waves, but there is significant scatter in their data with respect to the relationship between delay time and differential t^*. Possibly because of this scatter, they do not attempt to solve for Q. Global models [*Romanowicz*, 1995; *Bhattacharyya et al.*, 1996; *Reid et al.*, 2001] are consistent with the above studies and also lack the resolution to quantify changes in temperature, partial melt and composition in the upper mantle beneath the Rocky Mountains.

In this paper, we measure the integrated differential attenuation of teleseismic S-phases, δt^* [*Sheehan and Solomon*, 1992], and correct for sedimentary basin reverberations. This measurement along with an a priori velocity model and ray path modeling is used to derive the shear wave attenuation structure in the upper mantle. This information is coupled with the Lee and Grand shear wave velocity model [1996] to identify regions of compositional and thermal variability. Karato's shear velocity - temperature derivative relationship [1993] is applied to estimate the mantle thermal component of isostatic compensation while an analysis is performed using the residual topography to estimate the best relationship between density and unrelaxed shear velocity, $\partial \ln\rho / \partial \ln V_S$, and better constrain the likely compositions. The mantle component of isostatic compensation is combined with estimates of compensation due to changes in crustal thickness using the model of Li et al. [2002] to evaluate overall isostatic compensation.

2. δt^* MEASUREMENT

The RMF seismic dataset consists of a two dimensional array of 37 broadband, multicomponent seismometers , 26 of which were used for this study (Figure 2, Table 1), deployed for a period of nearly seven months during 1992 [*Sheehan et al.*, 1995; *Lerner-Lam et al.*, 1998]. Twenty-seven stations were Guralp CMG3-ESP seismometers with a 30 second corner period, two were Guralp CMG3 seismometers with a 10 second corner period, and eight were Streckeisen STS-2 seismometers with a 120 second corner period. The instrument response of the seismometers is flat below the corner period. Events are initially extracted based on the following criteria:

$$65 < d < 85 \;\&\; m_b > 5.6$$
$$45 < d < 65 \;\&\; m_b > 5.4$$
$$30 < d < 45 \;\&\; m_b > 5.3$$

where d is the epicentral distance in degrees and m_b is the body wave magnitude. All waveforms are visually inspected before picking windows for signal and noise (Figure 3a). Waveforms with no recognizable S phase are removed. The resulting dataset consists of 380 S-wave traces from 37 events (Figure 4, Table 2).

Each waveform undergoes conditioning before the calculation of δt^*. The channels are rotated to obtain the transverse component so as to isolate SH motion and minimize S to P conversions. The waveforms are band pass filtered to between 0.005 and 0.4 Hz and cropped to a 200 second window surrounding the hand picked S arrival. The waveform's trend and mean are removed, after which a 10% cosine taper is applied. The stations instrument response is removed and then the waveform is reconvolved with a common instrument response, that of the CMG-3 ESP broadband seismometer. The waveform is further reduced to a 30 second window centered on the S-pulse and multiplied by a gaussian taper. Larger windows and less severe tapers result in lower signal to noise ratios which degrades the measurement of δt^*. A multi-taper spectral analysis [*Percival and Walden*, 1993] with a time-bandwidth product of 3 is performed on the prepared time series to obtain the station spectra (Figure 3b).

For our measurements, t^* for a given signal is measured relative to a reference spectrum. The reference spectrum is derived from a pseudo-source which is the alignment and stack of all signals for a given event. The spectra for the station trace and the reference trace (Figure 5a) are given by:

$$A_S(f) = G_S S(f) I_S(f) R_S(f) e^{-\pi f t_S^*} \quad (2)$$

$$A_R(f) = G_R S(f) I_R(f) R_R(f) e^{-\pi f t_R^*} \quad (3)$$

where f is the frequency, G is the geometrical spreading, S is the source function, I is the instrument response, R is the crustal response, and $e^{-\pi f t^*}$ results from the energy loss along the ray's path from source to receiver. The subscripts S and R refer to the station and reference respectively. To find δt^*, we look at the ratio of spectral amplitudes, $A_S(f)/A_R(f)$. Relative t* is calculated for a given event to facilitate the cancellation of the source term in the spectral ratio. If the geometrical spreading is frequency independent, δt^* will not be a function of G. The instrument response cancels because we have removed the station instrument response, $I_S(f)$, and reconvolved the waveform with a common instrument response, $I_R(f)$. At this point, the crustal response terms are removed. Synthetic tests are performed to further examine the

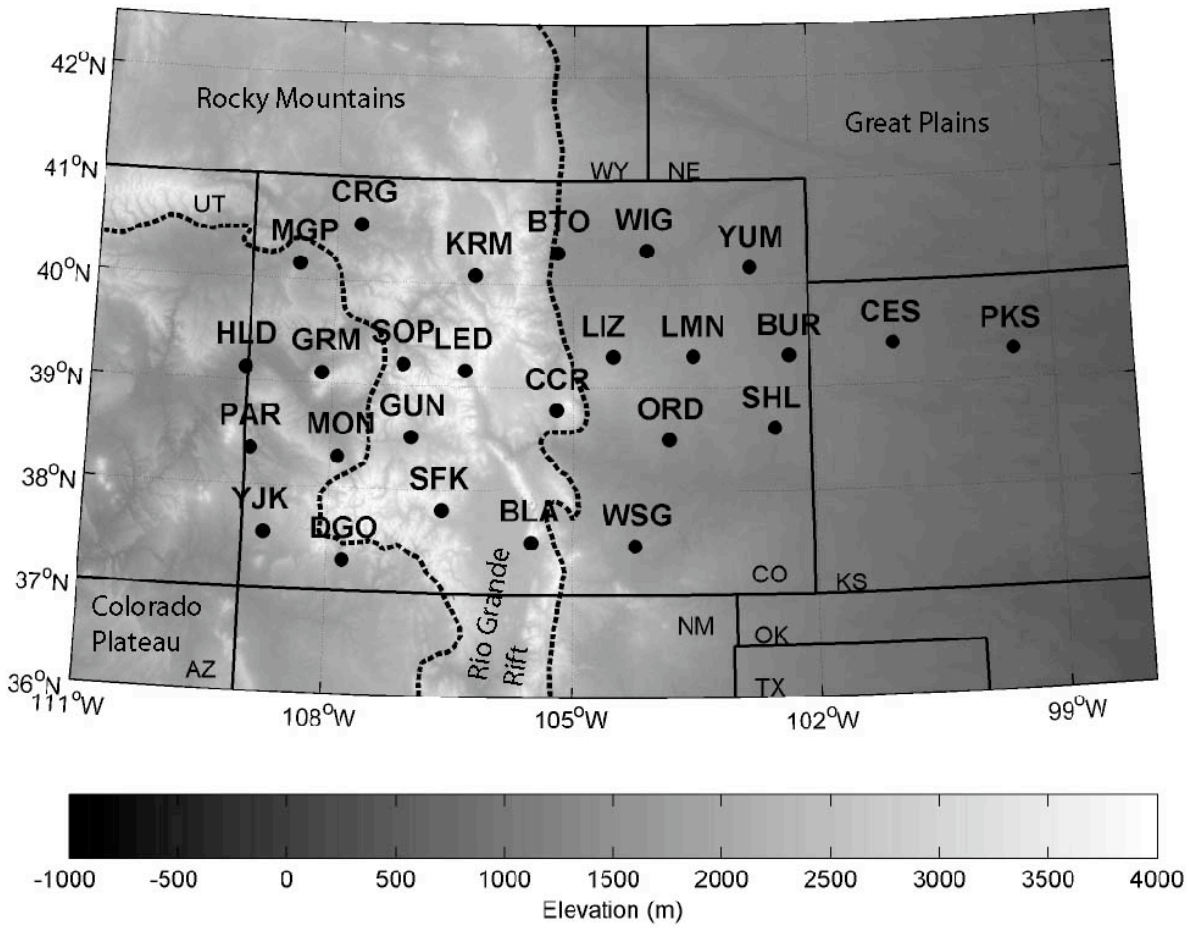

Figure 2. Seismic stations of the Rocky Mountain Front seismic experiment (RMF) used in this study on gray-scale topographic relief map. Stations are denoted by filled circles and a three letter station code. Geologic provinces are separated by thick dashed lines.

contribution of crustal response terms (Appendix 1.1) and a correction to δt^* is made using estimated basin thicknesses, shear velocities and impedance contrasts. The remaining spectral ratio is

$$\frac{A_S(f)}{A_R(f)} = e^{-\pi f(t_S^* - t_R^*)}. \qquad (4)$$

Solving for δt^*, we have

$$\delta t^* = t_S^* - t_R^* = \partial \left[\ln\left(\frac{A_S(f)}{A_R(f)} \right) \Big/ -\pi \right] \partial f \ . \qquad (5)$$

The slope of the curve between $\ln(A_S(f)/A_R(f))/(-\pi)$ and f is δt^*. We make δt^* measurements by finding the slope of the straight line that is fit to the curve of $\ln(A_S(f)/A_R(f))/(-\pi)$ vs. f over the frequency range 0.02 to 0.1 Hz (Figure 5b). This frequency range is used in the measurements for two reasons. The spectral energy at these frequencies is high, the spectral decay at higher frequencies can be dominated by scattering attenuation, and the spectral energy at lower frequencies can be contaminated by decreased sensitivity of the sensors.

The total number of traces for which δt^* is calculated is 380 (Table 3). The number of traces originating from the northwest is 280, the northeast, 25, the southeast, 75, and southwest, 0. After removing apparent δt^* due to basin reflections (Appendix 1.1), the variance of δt^* is 0.63 seconds. Appendix 1.2 uses synthetics to determine that 75% of this variance could be due to normally distributed random noise. This may seem excessive but Appendix 2 shows that a properly weighted inversion can produce a reasonable model.

Figure 6 is an average δt^* map for events originating from the northwest (top) and southeast (bottom) for uncorrected (left) and basin corrected (right) δt^* values. All δt^* values for events originating from a given direction for a given station are weighted by the inverse of the standard deviation of δt^* error due to normally distributed random noise (Appendix 1.2) and averaged, and the resulting weighted average is placed at the station location. The basin corrections tend to be negative resulting in an increase in δt^* in the basins after the correction is applied. Observations of the spatial distribution of δt^* in

Table 1. Station Information

Station Name	Latitude	Longitude	Elevation (km)	Sediment Thickness (km)	Sediment Shear Vel. (km/s)	Basin Reflection Coefficient
BLA	37.54	-105.58	2.72	0.0		
BTO	40.38	-105.20	1.73	1.4	2.15	-0.29
BUR	39.38	-102.35	1.26	1.9	2.15	-0.29
CCR	38.77	-105.22	2.68	0.0		
CES	39.38	-101.05	0.94	0.0		
CRG	40.54	-107.70	2.07	5.1	1.98	-0.32
DGO	37.30	-107.81	2.43	2.4	2.28	-0.22
GRM	39.10	-108.13	2.37	2.4	1.98	-0.31
GUN	38.50	-107.00	2.66	0.0		
HLD	39.23	-109.08	1.50	0.0		
KRM	40.08	-106.24	2.53	1.8	2.15	-0.29
LED	39.15	-106.35	3.37	0.0		
LIZ	39.35	-104.54	1.99	4.1	2.15	-0.29
LMN	39.41	-103.62	1.63	2.9	2.15	-0.29
MGP	40.15	-108.46	1.93	2.2	1.98	-0.32
MON	38.41	-107.99	2.39	0.6	2.28	-0.22
ORD	38.50	-103.80	1.47	2.0	2.15	-0.29
PAR	38.33	-108.98	2.05	4.0	2.28	-0.22
PKS	39.25	-99.53	0.63	0.0		
SFK	37.80	-106.60	3.07	0.0		
SHL	38.60	-102.50	1.26	1.8	2.15	-0.29
SOP	39.21	-107.12	2.66	0.0		
WIG	40.32	-104.07	1.39	2.8	2.15	-0.29
WSG	37.47	-104.23	1.71	0.7	2.15	-0.29
YJK	37.54	-108.77	2.08	2.7	2.28	-0.22
YUM	40.16	-102.78	1.27	2.1	2.15	-0.29

Table 1. Station information. Station designation, latitude, longitude, elevation, sediment thickness [*Sheehan et al.*, 1995; *Burchfiel*, 1992], velocity, and reflection coefficient. Please see Appendix 1.1 for information about velocity and reflection coefficient.

dependence on backazimuth are inconclusive. It appears possible that high δt^* moves to the northwest when examining events from the southeast and to the southeast for events from the northwest. The lack of an obvious pattern may mean that the measurements have considerable error or that the distribution of attenuation in the upper mantle is sufficiently complex to make the examination of these δt^* maps inconclusive.

3. δQ^{-1} INVERSION

Solving for differential attenuation is a relatively straight forward inverse problem. Relative t^* is related to attenuation, Q^{-1}, through the following expression:

$$\delta t^* = \int_S Q_R^{-1} d\tau_R - \int_S Q_S^{-1} d\tau_S \qquad (6)$$

where τ is the travel time. As before, the subscripts S and R refer to the station and reference respectively. δt^* is the difference in the integrated effect of energy loss along the ray path between a reference trace and a station trace. In order to turn (6) into a tractable inverse problem, we assume that $d\tau_R = d\tau_S = d\tau$ such that

$$\delta t^* = \int \Delta Q^{-1} d\tau \qquad (7)$$

where

$$\Delta Q^{-1} = Q_R^{-1} - Q_S^{-1}. \qquad (8)$$

We use the δt^* measurements, the ray path derived from 2-D ray tracing and the western U.S. one dimensional velocity model, TNA [*Grand and Helmberger*, 1984], to invert for variations in Q^{-1} in the study area. We assume that variations in Q^{-1} between seismic rays for a given event are confined to the upper 400 km of the mantle.

Singular value decomposition [*Menke*, 1984] is used to do the inversion. Equation 7 can be written in the form

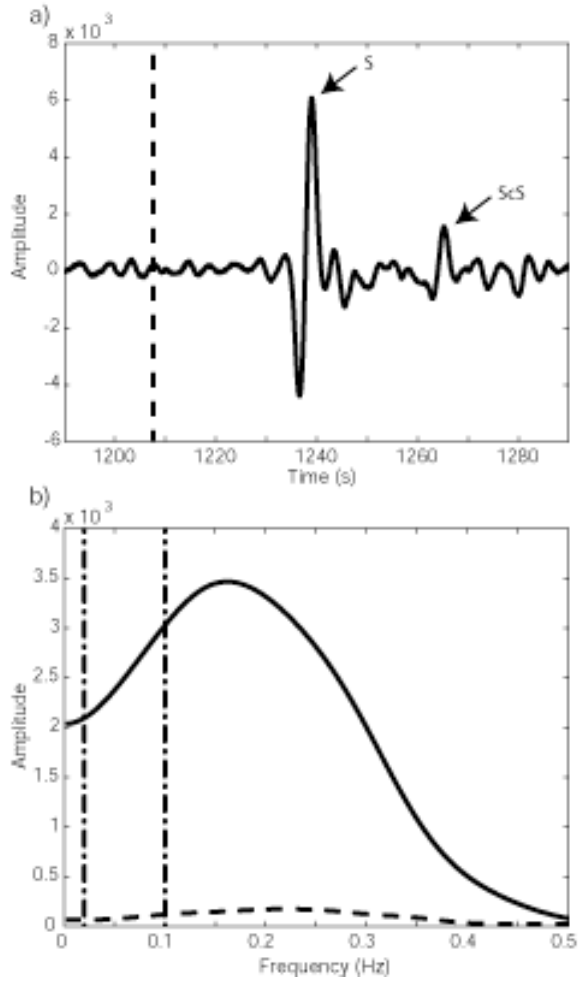

Figure 3. Example time series (a) and associated spectra for signal and noise (b). (a) Seismic phases S and ScS are denoted for reference. The dashed vertical line is the location of the center of the 30 second time window for the noise. This time series was recorded at station DGO and is from a magnitude 5.7 earthquake in northern Japan (backazimuth of 318 degrees, distance of 76 degrees, and depth of 317 km). (b) Signal spectra (solid line) and pre-event noise spectra (dashed line). Signal to noise ratio is 28.5. The dotted lines indicate the frequency range over which the δt* measurement is made.

$$\delta t_i^* = \sum_j d\tau_{ij} \Delta Q_i^{-1} \tag{9}$$

where δt_i^* is the data vector consisting of i δt^* measurements, ΔQ_j^{-1} is the model vector of differential attenuation in each of j blocks, and $d\tau_{ij}$ is the data kernel matrix with ray path travel time information. Singular value decomposition seeks a solution to

$$\Delta Q^{-1} = d\tau^{-1} \delta t^* \tag{10}$$

where

$$d\tau^{-1} = D_p \Lambda_p M_p^T . \tag{11}$$

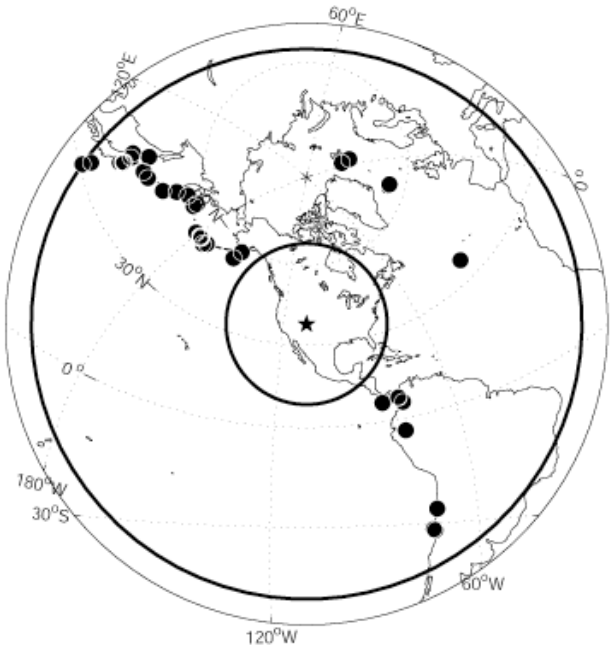

Figure 4. Locations of earthquakes used in this study (filled circles). Most of the events originate from either the northwest or southeast. Thick solid black circles are 30 and 80 degrees distant from the center of the RMF seismic array.

Equation 11 is referred to as the natural generalized inverse. It is composed of D, a matrix of eigenvectors that span the data space, M, a matrix of eigenvectors that span the model space, and Λ, a matrix of eigenvalues whose diagonal elements are the singular values. The parameter p corresponds to the number of largest singular values kept when calculating $d\tau^{-1}$. In our case we have chosen to use all singular values within two orders of magnitude of the largest. Using only the largest p singular values is referred to as a truncated singular value decomposition (TSVD) and is equivalent to damping the solution, reducing model variance at the expense of model resolution.

In order to reduce the adverse effects of significant random noise, we use a weighted TSVD where the weights, W, are the inverse of the standard deviation of δt^* error due to normally distributed random noise (Appendix 1.1) [*Meju*, 1994]. Multiplying both sides of (9) by W, we have

$$W\delta t^* = Wd\tau\Delta Q^{-1} . \tag{12}$$

We now seek a solution to

$$\Delta Q^{-1} = \left(Wd\tau\right)^{-1} W\delta t^* . \tag{13}$$

The eigenvectors and eigenvalues of equation (11) are now found for the quantity $(Wd\tau)^{-1}$.

The inversion is solved for average attenuation values in 100 × 100 × 100 km bins extending from 113.7°W to 96°W, 33.7°N to 43.6°N, and 0 to 400 km depth. The bins are

Table 2. Event Information

Event #	Origin time	Latitude	Longitude	Depth (km)	Magnitude	σ(δt*) / NS
21	5/30/1992 (151) 12:42:03.500	30.69	141.59	20	5.9	3.7
39	6/03/1992 (155) 6:10:54.300	51.13	178.74	22	5.9	3.2
64	6/16/1992 (168) 5:51:03.700	45.70	142.26	317	5.7	3.6
68	6/21/1992 (173) 10:52:42.400	-26.50	289.34	39	5.7	4.8
77	6/24/1992 (176) 12:11:26.000	51.50	186.55	33	5.7	3.8
82	6/26/1992 (178) 11:32:27.100	6.13	277.65	10	5.8	5.1
138	7/10/1992 (192) 9:31:27.500	44.70	149.48	20	6.2	2.8
142	7/12/1992 (194) 11:08:55.300	41.46	142.03	64	6.0	3.2
146	7/13/1992 (195) 15:34:04.500	51.17	157.63	45	5.7	5.3
147	7/13/1992 (195) 18:11:33.700	-3.92	283.40	97	6.1	3.4
161	7/18/1992 (200) 8:36:58.700	39.42	143.33	29	6.2	2.8
165	7/18/1992 (200) 10:20:11.900	39.44	143.03	27	6.1	2.9
171	7/18/1992 (200) 13:56:54.400	39.48	142.96	27	5.8	3.3
180	7/20/1992 (202) 7:46:46.700	78.56	5.52	10	5.7	3.0
189	7/25/1992 (207) 2:53:28.300	38.73	143.01	17	5.9	2.6
202	7/29/1992 (211) 4:30:47.700	39.50	143.50	16	5.9	3.6
229	8/11/1992 (224) 15:14:55.100	32.54	141.64	16	5.8	3.7
233	8/15/1992 (228) 19:02:09.100	5.11	284.39	119	5.7	3.8
239	8/19/1992 (232) 0:57:40.200	50.50	185.08	10	6.2	3.4
251	8/24/1992 (237) 6:59:39.900	41.98	140.66	121	6.2	3.6
293	9/09/1992 (253) 13:08:54.800	76.21	7.29	24	5.7	4.2
306	9/14/1992 (258) 20:33:30.500	54.32	166.67	38	5.5	5.5
323	9/26/1992 (270) 5:45:50.600	64.78	342.41	10	5.5	3.5
326	9/27/1992 (271) 17:48:13.000	53.93	202.70	33	5.8	3.6
330	9/30/1992 (274) 3:27:59.100	51.41	181.37	26	5.9	4.1
331	9/30/1992 (274) 5:34:00.300	51.28	181.96	33	6.1	3.2
333	9/30/1992 (274) 9:42:50.900	51.15	181.83	14	5.8	3.1
335	10/01/1992 (275) 5:02:34.100	51.12	182.00	15	5.9	4.2
342	10/08/1992 (282) 16:34:53.200	51.15	182.13	21	5.6	4.0
355	10/17/1992 (291) 8:32:40.500	6.85	283.19	14	6.2	2.9
359	10/18/1992 (292) 15:11:59.100	7.08	283.14	10	6.6	3.2
371	10/20/1992 (294) 4:40:01.700	55.52	166.30	27	5.7	5.4
405	11/04/1992 (309) 21:32:33.900	-31.57	288.44	19	5.8	2.4
412	11/10/1992 (315) 9:58:10.800	51.49	182.39	33	5.8	5.7
436	11/28/1992 (333) 3:13:33.300	-31.33	288.01	12	5.8	3.3
437	11/30/1992 (335) 9:32:37.500	35.69	325.42	20	6.1	4.7
442	12/07/1992 (342) 2:11:42.300	43.95	147.15	45	5.8	4.4

Table 2. Event information from NEIC. Event #, origin time: date, Julian day and time, latitude, longitude, depth, magnitude (m_b), and the slope of the relationship between the standard deviation of δt^* and the synthetic noise to signal ratio, σ(δt*) / NS, determined for each event (Appendix 1.2).

offset by 10 km in each direction and the inversion is repeated, producing a total of 1000 inversions. This procedure is done twice. In the first iteration, a solution for the event mean is included. In the second, the 1000 estimates of the event mean from the first iteration are averaged, removed from the δt^* data, and the inversion is performed again without the solution for the event mean. The inversions are sequentially combined, generating a psuedo-effective resolution of 10 km, and smoothed by convolving the model with a 200 × 200 × 50 km unit box.

For regions in the model with a resolution derived from the resolution matrix (A2.1) greater than 0.3, the range in ΔQ^{-1} is 0.04. The variance reduction of the corrected δt^* data due to the resulting model is 10%, a value that is expected given the amount of random error in δt^* (Appendix 2). Romanowicz [1995] reports a variance

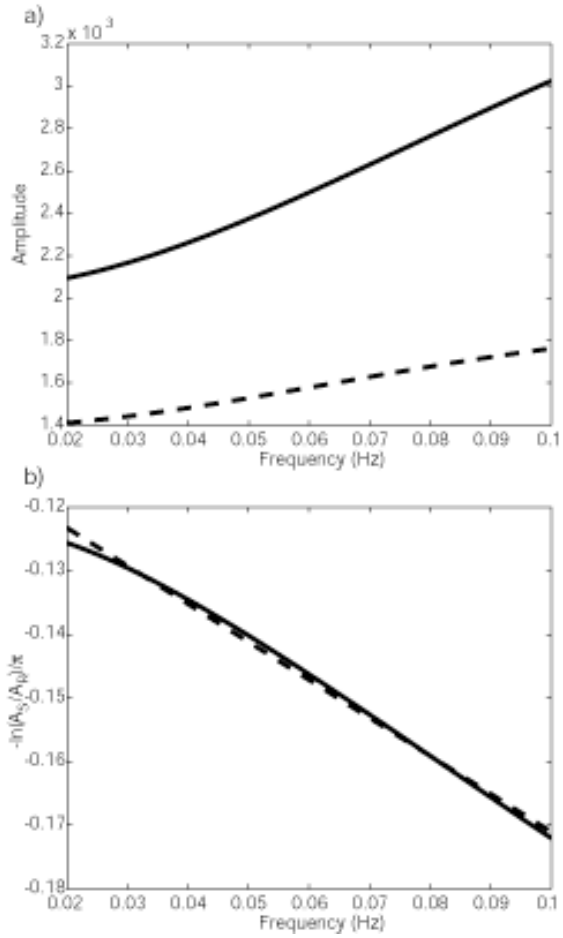

Figure 5. Example spectra for the signal (solid line) and reference (dashed line) (a) and spectral ratio (dashed – dot line) with linear fit (b). (a) The signal spectrum is that shown in Figure 3b limited to the frequency range 0.02 to 0.1 Hz. The reference spectrum is the average of spectra from all stations present for a given event. (b) The dashed dot line is the natural log of the ratio of amplitudes between the station and the reference divided by -π. The solid line is the linear fit to the dashed dot line over the frequency range 0.02 to 0.1 Hz. For this example, δt^* is –0.59. The difference to the value given in Table 3 is due to the removal of the event mean.

reduction of 49% for her global model of upper mantle shear wave attenuation, a value approaching the variance reduction achieved in velocity tomography. Reid et al. [2001] generate a variance reduction of 23% in their upper mantle shear wave Q model while their velocity model is able to produce a variance reduction of 67%.

The ray path travel times are calculated using a one-dimensional velocity model. Because of this assumption, the resulting Q^{-1} model is incorrect by an amount approximately equal to the fractional difference between the one-dimensional velocity model and the true Earth velocity structure. For example, where the Earth velocities are 5% lower than the one-dimensional velocities, the actual Q^{-1} model should also be reduced by 5%. A competing effect not accounted for is that due to focusing and defocusing of the seismic energy from lateral velocity

Table 3. δt^* Data and Information

Station Name	Event Num	Original δt^*	δt^* corrected	δt^* correction	SN
MGP	21	0.46	0.63	0.17	14.5
CRG	21	-1.24	-0.69	0.55	15.7
HLD	21	0.29	0.29	0.00	39.3
GRM	21	-0.91	-0.68	0.22	14.1
MGP	39	0.12	0.24	0.12	18.5
CRG	39	-0.88	-0.40	0.48	9.3
HLD	39	0.03	0.03	0.00	18.7
GRM	39	-0.14	0.03	0.17	13.4
PAR	39	-0.69	-0.41	0.29	13.7
KRM	39	0.05	0.07	0.03	22.9
SOP	39	-0.47	-0.54	0.00	30.2
MON	39	0.82	0.80	-0.02	14.3
YJK	39	-0.78	-0.66	0.12	26.7
BTO	39	0.04	0.02	-0.02	46.3
GUN	39	0.07	0.07	0.00	21.3
DGO	39	-1.61	-1.55	0.06	15.0
WIG	39	-0.07	0.15	0.22	10.7
YUM	39	0.10	0.16	0.06	19.4
LMN	39	-1.13	-0.88	0.25	13.0
CES	39	1.04	1.04	0.00	30.9
PKS	39	0.43	0.43	0.00	41.5
MGP	64	-0.21	-0.03	0.18	14.8
CRG	64	-1.24	-0.94	0.31	18.8
HLD	64	0.10	0.10	0.00	22.8
GRM	64	-0.30	-0.06	0.24	11.3
PAR	64	-0.35	-0.06	0.29	39.8
BTO	64	0.09	0.11	0.01	31.3
MON	64	0.35	0.34	-0.01	41.9
YJK	64	-0.46	-0.30	0.16	18.0
LED	64	-1.66	-1.66	0.00	4.5
GUN	64	0.35	0.35	0.00	22.4
DGO	64	-0.50	-0.40	0.10	28.5
CCR	64	0.31	0.31	0.00	41.4
YUM	64	0.00	0.11	0.11	16.5
LMN	64	0.03	0.33	0.30	11.9
BLA	64	0.44	0.44	0.00	2.1
ORD	64	-0.50	-0.41	0.09	0.8
BUR	64	0.21	0.28	0.07	4.2
CES	64	0.41	0.41	0.00	14.3
PKS	64	-0.14	-0.14	0.00	12.5

Table 3. δt* data and information. Station name, Event number from NEIC, the original t*, corrected t*, and t* correction, and the waveforms signal to noise ratio.

heterogeneities. Our analysis of this phenomenon suggests that when using our technique for measuring t^* and the velocity perturbations of Lee and Grand, Q^{-1} will decrease by less than 5% in regions of low velocity (focusing) and increase by less than 5% in regions of high velocity (defocusing). These regions will be flanked by decaying

Table 3. δt^* Data and Information (continued)

Station Name	Event Num	Original δt^*	δt^* corrected	δt^* correction	SN
PKS	68	0.48	0.48	0.00	17.6
WSG	68	0.18	0.19	0.01	42.6
CES	68	-0.68	-0.68	0.00	6.9
BUR	68	-0.92	-0.76	0.16	3.7
LMN	68	-1.60	-1.13	0.47	9.0
LIZ	68	-0.82	-0.15	0.68	7.3
YUM	68	-1.17	-0.95	0.22	17.1
GUN	68	0.25	0.25	0.00	12.2
YJK	68	-0.50	-0.24	0.26	9.9
LED	68	1.47	1.47	0.00	1.6
MON	68	-0.36	-0.35	0.00	7.2
WIG	68	-0.86	-0.43	0.44	12.9
BTO	68	0.28	0.36	0.07	4.7
PAR	68	0.10	0.55	0.44	6.9
GRM	68	0.23	0.62	0.39	14.6
KRM	68	1.02	1.19	0.16	4.9
HLD	68	-0.10	-0.10	0.00	6.1
CRG	68	-0.94	-0.39	0.55	23.8
MGP	68	0.01	0.33	0.32	37.8
CRG	77	-1.07	-0.58	0.49	18.1
HLD	77	0.02	0.02	0.00	11.6
PAR	77	0.04	0.39	0.34	11.5
GRM	77	0.03	0.28	0.25	11.9
KRM	77	-0.10	-0.02	0.08	11.0
YJK	77	0.58	0.75	0.17	16.6
MON	77	0.63	0.61	-0.01	22.9
BTO	77	0.12	0.13	0.01	13.2
GUN	77	0.40	0.40	0.00	11.4
LED	77	-0.58	-0.58	0.00	3.1
WIG	77	-0.77	-0.47	0.30	10.7
LIZ	77	-0.92	-0.38	0.54	21.2
YUM	77	-0.36	-0.24	0.12	8.4
LMN	77	-1.52	-1.18	0.33	15.7
BUR	77	0.07	0.14	0.08	8.1
WSG	77	1.13	1.12	-0.02	8.6
CES	77	0.40	0.40	0.00	12.2
PKS	77	-0.35	-0.35	0.00	30.6
PKS	82	-1.20	-1.20	0.00	7.6
WSG	82	-0.03	-0.03	0.01	6.4
CES	82	-2.61	-2.61	0.00	5.3
BUR	82	-0.96	-0.85	0.11	5.3
DGO	82	2.24	2.36	0.13	4.0
WIG	82	-1.48	-1.19	0.29	3.6
LED	82	0.76	0.76	0.00	8.2

Table 3. δt^* Data and Information (continued)

Station Name	Event Num	Original δt^*	δt^* corrected	δt^* correction	SN
YJK	82	-0.03	0.14	0.17	24.8
BTO	82	-0.36	-0.31	0.05	3.0
KRM	82	-0.46	-0.35	0.11	3.9
GRM	82	1.65	1.91	0.26	4.2
HLD	82	0.98	0.98	0.00	7.9
CRG	82	-0.68	-0.42	0.26	6.4
MGP	82	0.29	0.51	0.22	5.8
CRG	138	-0.51	-0.32	0.19	10.1
GRM	138	-0.72	-0.70	0.02	12.6
PAR	138	0.01	0.04	0.03	9.5
KRM	138	0.17	0.17	0.00	1.7
SOP	138	-0.43	-0.41	0.00	15.1
MON	138	-0.09	-0.10	-0.01	20.3
BTO	138	-0.28	-0.29	-0.01	23.3
LED	138	0.51	0.51	0.00	17.5
WIG	138	0.63	0.65	0.02	11.6
SFK	138	-0.06	-0.06	0.00	16.9
CCR	138	0.75	0.75	0.00	18.3
YUM	138	0.30	0.30	0.00	12.5
LMN	138	-0.39	-0.37	0.02	7.4
BLA	138	-0.34	-0.34	0.00	3.4
PKS	138	0.15	0.15	0.00	17.0
MGP	142	-0.10	0.10	0.20	20.4
CRG	142	-0.97	-0.68	0.29	54.9
HLD	142	0.59	0.59	0.00	35.1
GRM	142	-0.42	-0.16	0.25	18.3
PAR	142	0.19	0.49	0.30	29.6
SOP	142	-0.23	-0.35	0.00	29.2
MON	142	0.74	0.72	-0.01	25.5
BTO	142	-0.20	-0.18	0.01	25.7
LED	142	0.30	0.30	0.00	29.5
WIG	142	-0.69	-0.39	0.29	18.9
SFK	142	-0.15	-0.15	0.00	28.0
CCR	142	1.02	1.02	0.00	34.6
LIZ	142	-1.48	-1.02	0.46	16.7
YUM	142	-0.40	-0.28	0.12	24.1
LMN	142	-0.94	-0.62	0.32	18.6
BLA	142	0.02	0.02	0.00	34.3
WSG	142	2.62	2.60	-0.02	2.8
CES	142	-0.89	-0.89	0.00	9.5
PKS	142	-0.94	-0.94	0.00	25.4
CRG	146	-0.34	0.04	0.38	13.4
HLD	146	0.64	0.64	0.00	5.8
KRM	146	-1.47	-1.29	0.18	12.0

oscillations of high and low Q^{-1}. Work by Allen et al. [1999] indicates that focusing/defocusing effects on t^* in the vicinity of the Icelandic plume could be more than two orders of magnitude larger than those determined here. The difference is primarily due to the potentially small radius of the Iceland plume, 100 km, its vertical orientation, and its large shear velocity anomaly, -12%. We calculate that the combined errors due to the focusing/defocusing and ray path travel time effects are minimal.

Figure 7 provides horizontal slices of the resulting differential shear wave attenuation model. When basin corrections are not applied, the negative attenuation

Table 3. δt^* Data and Information (continued)

Station Name	Event Num	Original δt^*	δt^* corrected	δt^* correction	SN
SOP	146	-0.08	-0.16	0.00	30.3
BTO	146	0.06	0.15	0.09	37.0
MON	146	0.75	0.76	0.01	10.1
LED	146	2.01	2.01	0.00	6.1
WIG	146	-1.43	-1.01	0.42	11.7
CCR	146	1.28	1.28	0.00	13.4
LIZ	146	-1.91	-1.33	0.57	12.1
SFK	146	-0.22	-0.22	0.00	12.2
YUM	146	-0.94	-0.70	0.24	5.7
LMN	146	-1.04	-0.59	0.45	4.5
BLA	146	1.08	1.08	0.00	11.4
ORD	146	0.07	0.28	0.21	9.9
PKS	146	-0.69	-0.69	0.00	7.6
PKS	147	0.29	0.29	0.00	38.8
WSG	147	0.53	0.50	-0.03	19.1
CES	147	-2.04	-2.04	0.00	19.2
ORD	147	0.58	0.64	0.06	4.8
BLA	147	-0.60	-0.60	0.00	13.2
LMN	147	-0.72	-0.43	0.28	13.2
YUM	147	-0.71	-0.62	0.09	17.1
CCR	147	0.36	0.36	0.00	20.4
LIZ	147	0.15	0.61	0.46	13.1
WIG	147	-0.40	-0.15	0.25	13.7
LED	147	-0.17	-0.17	0.00	11.0
BTO	147	1.46	1.45	-0.01	15.0
SOP	147	-0.07	-0.18	0.00	15.7
KRM	147	0.02	0.06	0.04	14.7
GRM	147	-0.12	0.09	0.21	16.0
HLD	147	-0.19	-0.19	0.00	20.6
MGP	147	0.32	0.47	0.15	14.3
MGP	161	-0.03	-0.02	0.01	32.6
HLD	161	0.36	0.36	0.00	96.8
KRM	161	0.21	0.20	-0.01	71.8
SOP	161	0.29	0.29	0.00	66.8
MON	161	0.10	0.08	-0.01	70.3
BTO	161	-0.24	-0.27	-0.03	84.8
LED	161	0.16	0.16	0.00	41.1
GUN	161	0.58	0.58	0.00	15.6
WIG	161	-0.19	-0.14	0.05	48.4
SFK	161	0.17	0.17	0.00	44.3
LIZ	161	-0.67	-0.48	0.19	9.3
YUM	161	0.04	0.04	0.00	26.2
LMN	161	-0.37	-0.31	0.06	47.6
CRG	161	-0.87	-0.53	0.34	27.8

Table 3. δt^* Data and Information (continued)

Station Name	Event Num	Original δt^*	δt^* corrected	δt^* correction	SN
ORD	161	0.33	0.32	-0.01	27.3
WSG	161	0.72	0.70	-0.02	17.8
PKS	161	0.32	0.32	0.00	42.3
MGP	165	0.17	0.23	0.06	2.8
CRG	165	-0.61	-0.15	0.46	6.3
HLD	165	2.41	2.41	0.00	6.0
KRM	165	0.45	0.43	-0.02	5.6
SOP	165	-0.41	-0.49	0.00	3.6
MON	165	0.82	0.79	-0.03	6.9
BTO	165	0.08	0.03	-0.05	6.8
LED	165	0.72	0.72	0.00	2.9
GUN	165	0.88	0.88	0.00	3.2
DGO	165	-3.54	-3.51	0.03	7.0
WIG	165	-0.87	-0.70	0.17	3.6
SFK	165	0.70	0.70	0.00	7.4
YUM	165	-0.18	-0.16	0.02	5.3
LMN	165	-0.39	-0.19	0.20	8.1
PKS	165	-0.17	-0.17	0.00	2.4
MGP	171	-0.18	0.01	0.19	12.8
HLD	171	0.62	0.62	0.00	20.5
SOP	171	0.00	-0.11	0.00	3.2
MON	171	0.89	0.87	-0.02	15.1
BTO	171	-0.35	-0.35	0.00	18.9
LED	171	0.83	0.83	0.00	18.1
GUN	171	0.68	0.68	0.00	10.0
WIG	171	-0.98	-0.68	0.29	26.1
SFK	171	-0.23	-0.23	0.00	11.3
YUM	171	-0.72	-0.61	0.11	9.5
LMN	171	-1.25	-0.92	0.33	20.6
PKS	171	0.53	0.53	0.00	7.3
YUM	180	-0.13	0.14	0.27	15.1
WIG	180	-0.07	0.30	0.37	11.2
PKS	180	0.03	0.03	0.00	28.2
BTO	180	0.37	0.52	0.15	55.0
CRG	180	0.01	0.26	0.25	39.4
KRM	180	0.07	0.30	0.23	45.2
MGP	180	-0.65	-0.30	0.34	54.4
LED	180	-0.07	-0.07	0.00	41.4
ORD	180	0.30	0.55	0.25	33.9
GRM	180	-0.17	0.20	0.37	44.7
HLD	180	-0.53	-0.53	0.00	83.4
GUN	180	-3.83	-3.83	0.00	6.2
MON	180	-0.13	-0.09	0.04	85.3
WSG	180	0.14	0.20	0.07	46.4

anomalies correlate very well with the positions of the basins. The primary feature of this corrected model is the large relative attenuation trending north-northwest directly beneath the eastern Colorado Rockies. This feature extends to around 150 km depth and coincides with a modest decrease in shear wave velocity (Figure 1). An anomalous region exists just to the west where a decrease in attenuation coincides with the lowest velocities. Is this relationship a consequence of the high temperature side of an attenuation peak or compositional variability? At greater depths, the correlation to features at shallow levels disappears.

Table 3. δt^* Data and Information (continued)

Station Name	Event Num	Original δt^*	δt^* corrected	δt^* correction	SN
SFK	180	0.01	0.01	0.00	20.0
MGP	189	0.02	0.15	0.13	6.6
HLD	189	0.41	0.41	0.00	19.1
GRM	189	-0.31	-0.12	0.18	15.7
KRM	189	0.51	0.53	0.02	6.8
MON	189	0.32	0.29	-0.03	17.3
BTO	189	-0.49	-0.52	-0.03	7.6
WIG	189	-0.75	-0.52	0.23	10.0
SFK	189	0.13	0.13	0.00	47.9
LIZ	189	-1.51	-1.07	0.43	7.4
LMN	189	-0.38	-0.11	0.26	4.7
BUR	189	0.04	0.06	0.02	7.9
CES	189	-0.72	-0.72	0.00	6.7
MGP	202	0.08	0.24	0.16	22.1
HLD	202	0.54	0.54	0.00	33.2
GRM	202	-0.20	0.01	0.21	32.7
PAR	202	-0.71	-0.41	0.31	108.9
KRM	202	0.52	0.59	0.07	45.1
YJK	202	0.04	0.18	0.14	17.9
BTO	202	-0.17	-0.14	0.02	79.7
WIG	202	-0.68	-0.43	0.25	17.0
SFK	202	-0.06	-0.06	0.00	59.1
LIZ	202	-1.55	-1.06	0.49	17.3
BUR	202	0.19	0.26	0.07	16.2
CES	202	-0.49	-0.49	0.00	24.4
MGP	229	0.21	0.41	0.20	51.2
GRM	229	-0.38	-0.14	0.24	70.5
PAR	229	-0.23	0.07	0.30	46.2
KRM	229	0.47	0.58	0.11	12.1
MON	229	0.11	0.12	0.01	55.1
SOP	229	-0.16	-0.22	0.00	23.9
BTO	229	-0.20	-0.14	0.06	133.2
LED	229	-0.62	-0.62	0.00	30.7
SHL	233	0.79	0.97	0.18	3.2
BUR	233	-0.52	-0.34	0.18	2.7
YUM	233	-0.27	-0.03	0.24	2.7
WIG	233	0.93	1.37	0.44	3.8
BTO	233	1.65	1.73	0.08	8.9
MON	233	-1.77	-1.77	0.01	8.7
GRM	233	-1.68	-1.27	0.40	5.6
PAR	239	-0.22	-0.05	0.18	4.0
KRM	239	0.86	0.93	0.06	8.1
SOP	239	-1.44	-1.49	0.00	9.9
MON	239	0.13	0.14	0.00	5.8

Table 3. δt^* Data and Information (continued)

Station Name	Event Num	Original δt^*	δt^* corrected	δt^* correction	SN
BTO	239	-0.02	0.01	0.03	19.2
LED	239	-0.19	-0.19	0.00	8.4
SFK	239	-1.13	-1.13	0.00	7.2
WIG	239	0.56	0.71	0.15	5.2
LMN	239	-0.07	0.09	0.16	5.7
SHL	239	-0.12	-0.06	0.06	10.6
PKS	239	1.14	1.14	0.00	11.7
MGP	251	-0.24	-0.01	0.23	18.4
HLD	251	0.05	0.05	0.00	28.3
GRM	251	-0.18	0.11	0.29	39.5
KRM	251	1.20	1.30	0.10	11.0
SOP	251	-0.21	-0.35	0.00	25.7
MON	251	0.63	0.62	-0.01	19.2
LED	251	0.22	0.22	0.00	16.2
GUN	251	0.60	0.60	0.00	19.1
WIG	251	-0.84	-0.51	0.33	17.1
YUM	251	-0.43	-0.28	0.15	12.7
LMN	251	-0.81	-0.46	0.36	17.0
BUR	251	-0.96	-0.86	0.10	5.3
SHL	251	-0.16	-0.06	0.10	13.8
CES	251	-0.15	-0.15	0.00	4.4
PKS	251	0.05	0.05	0.00	20.1
KRM	293	0.73	0.81	0.08	3.7
LMN	293	-0.73	-0.43	0.30	3.7
GUN	293	-0.38	-0.38	0.00	11.2
BLA	293	0.63	0.63	0.00	4.6
GUN	306	0.66	0.66	0.00	5.7
SFK	306	-0.15	-0.15	0.00	4.4
LMN	306	-1.56	-1.26	0.31	7.4
BLA	306	1.17	1.17	0.00	2.5
PKS	306	0.23	0.23	0.00	14.3
BTO	323	0.44	0.44	0.00	4.1
SFK	323	-0.17	-0.17	0.00	6.3
MON	323	-0.19	-0.21	-0.01	3.6
MON	326	0.75	0.73	-0.02	11.5
BTO	326	0.20	0.21	0.00	15.7
GUN	326	0.88	0.88	0.00	8.6
SFK	326	1.21	1.21	0.00	3.0
LIZ	326	-1.38	-0.88	0.49	7.2
BLA	326	1.81	1.81	0.00	6.6
LMN	326	-1.72	-1.40	0.32	11.4
BUR	326	-1.48	-1.42	0.06	7.5
CES	326	-0.39	-0.39	0.00	4.4
MON	330	0.38	0.37	-0.01	9.9

4. THE PHYSICAL STATE OF THE UPPER MANTLE

To fully appreciate these results, attenuation measurements are combined with velocity measurements [*Roth et al.*, 2000; *Anderson*, 1989; *Nowick and Berry*, 1972]. This analysis can be used to estimate the temperature [*Karato*, 1993; *Sato and Ryan*, 1994; *Goes et al.*, 2000], percent partial melt [*Hammond and Humphreys*, 2000b; *Hammond and Humphreys*, 2000a; *Sato and Ryan*, 1994], and composition [*Karato and Jung*, 1998; *Duffy and Anderson*, 1989] of the material through which the seismic wave has passed. Most regional velocity studies have either

Table 3. δt^* Data and Information (continued)

Station Name	Event Num	Original δt^*	δt^* corrected	δt^* correction	SN
BTO	330	0.05	0.08	0.03	26.8
GUN	330	0.21	0.21	0.00	11.5
SFK	330	-0.33	-0.33	0.00	14.9
LIZ	330	-0.86	-0.43	0.43	8.2
LMN	330	-0.93	-0.60	0.34	6.3
BUR	330	-0.27	-0.17	0.10	10.1
CES	330	0.52	0.52	0.00	10.8
MON	331	1.01	1.01	0.00	31.5
BTO	331	-0.55	-0.53	0.02	31.0
GUN	331	0.13	0.13	0.00	14.8
SFK	331	0.08	0.08	0.00	21.8
LIZ	331	-0.88	-0.12	0.76	15.2
BLA	331	0.52	0.52	0.00	32.6
LMN	331	-1.58	-1.24	0.34	43.6
BUR	331	0.01	0.08	0.07	21.3
SHL	331	-0.37	-0.30	0.07	4.6
CES	331	0.79	0.79	0.00	21.5
MON	333	1.07	1.07	0.00	7.1
BTO	333	-0.25	-0.21	0.04	24.1
GUN	333	-0.24	-0.24	0.00	7.7
SFK	333	0.62	0.62	0.00	6.7
LIZ	333	-2.18	-1.40	0.78	21.5
BLA	333	0.15	0.15	0.00	5.1
LMN	333	-1.94	-1.59	0.35	5.7
BUR	333	0.50	0.59	0.10	14.8
SHL	333	2.10	2.19	0.10	2.9
CES	333	1.42	1.42	0.00	13.3
MON	335	0.15	0.13	-0.01	3.5
BTO	335	0.82	0.84	0.02	13.1
SFK	335	0.27	0.27	0.00	2.8
LIZ	335	-0.50	0.08	0.58	4.3
LMN	335	-1.42	-1.03	0.38	17.7
BUR	335	-0.49	-0.40	0.10	14.2
CES	335	1.75	1.75	0.00	6.5
MON	342	0.80	0.80	0.00	19.6
BTO	342	-0.87	-0.83	0.04	17.7
GUN	342	0.06	0.06	0.00	7.1
SFK	342	0.20	0.20	0.00	13.1
BLA	342	0.48	0.48	0.00	8.7
BUR	342	-1.07	-0.97	0.10	5.3
PKS	342	-0.36	-0.36	0.00	8.9
PKS	355	1.00	1.00	0.00	17.1
SHL	355	-1.46	-1.45	0.01	3.7
BUR	355	0.98	0.99	0.01	8.8

assumed a constant one dimensional Q profile with depth or assumed a simple relationship between velocity and Q [*Goes et al.*, 2000; *Sobolev et al.*, 1996]. Not knowing the true value of Q or its relationship to temperature, frequency, or velocity can be detrimental in the interpretation of sub-surface anomalies.

Table 3. δt^* Data and Information (continued)

Station Name	Event Num	Original δt^*	δt^* corrected	δt^* correction	SN
LMN	355	-1.12	-1.09	0.03	12.5
BTO	355	-0.95	-0.95	0.00	7.2
PKS	359	0.24	0.24	0.00	7.5
ORD	359	-0.59	-0.58	0.01	10.3
BLA	359	0.55	0.55	0.00	15.3
LMN	359	-0.31	-0.23	0.08	9.2
LIZ	359	-0.40	-0.22	0.18	9.2
BTO	371	0.61	0.66	0.04	35.3
LIZ	371	-0.75	-0.21	0.54	10.1
LMN	371	-0.63	-0.21	0.42	12.5
ORD	371	-0.35	-0.19	0.16	9.9
CES	371	-1.65	-1.65	0.00	6.6
PKS	371	-0.44	-0.44	0.00	14.8
PKS	405	0.05	0.05	0.00	3.7
LMN	405	-0.05	0.13	0.19	5.4
LIZ	405	-1.22	-0.88	0.34	4.6
BTO	405	0.28	0.26	-0.02	12.8
BTO	412	0.18	0.24	0.07	4.0
LIZ	412	0.79	1.66	0.86	1.7
LMN	412	-1.25	-0.67	0.58	2.3
PKS	412	-1.05	-1.05	0.00	2.2
SHL	436	1.49	1.54	0.05	6.4
SFK	436	-0.30	-0.30	0.00	27.0
LMN	436	-0.45	-0.19	0.26	16.0
BTO	436	0.05	0.05	0.00	18.5
LMN	437	0.50	0.77	0.27	3.7
BTO	437	1.63	1.67	0.04	2.6
SFK	437	-3.47	-3.47	0.00	2.1
BTO	442	0.63	0.66	0.02	3.4
SFK	442	1.56	1.56	0.00	2.0
LMN	442	-1.18	-0.84	0.34	5.6
SHL	442	-0.52	-0.44	0.09	1.6

Based on laboratory experiments [*Jackson*, 1993], attenuation is commonly observed to follow a power-law relationship where Q is proportional to angular frequency, w, raised to some positive power α. This model is believed to be due to the movement of dislocations having a range of thermally activated strengths and relaxation times and/or activation energies encompassing periods of at least 10^{-1} to 10^{2} seconds. Minster and Anderson [1981] proposed that there should be a minimum and maximum relaxation time spanning two to three decades in frequency. Above and below these values, attenuation is predicted to drop off to zero and produce an attenuation band or peak [*Nowick and Berry*, 1972]. Anderson and Given [1982] presented frequency dependent attenuation results in the mantle to which they ascribed an attenuation band, but their results as to the maximum and minimum relaxation times was inconclusive. From frequency dependent t^* measurements, Warren and Shearer [2000] are unable to conclusively observe an attenuation band but are able to state that

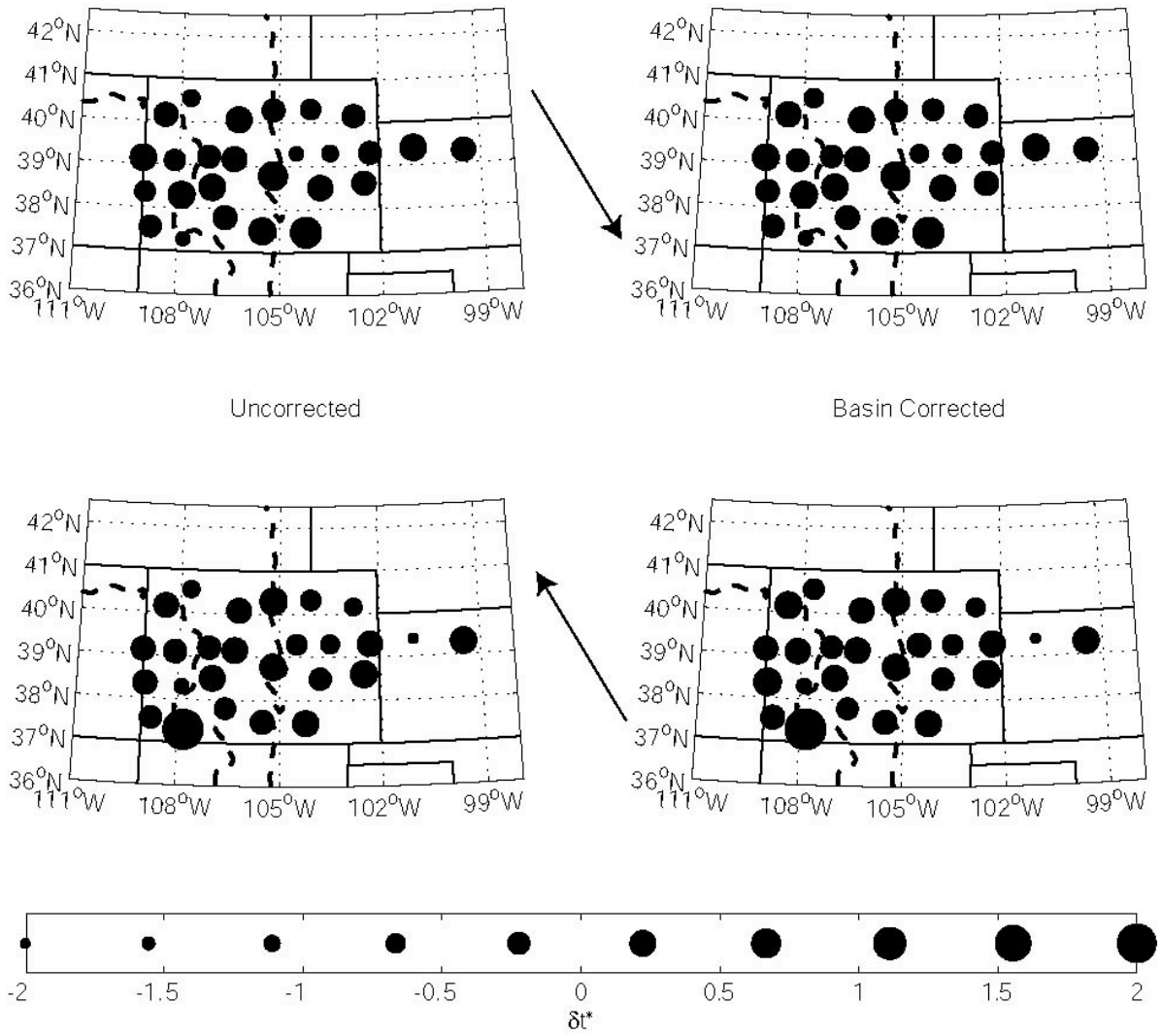

Figure 6. Weighted average δt* maps for events originating from the northwest (top) and southeast (bottom) for uncorrected (left) and sediment corrected (right) values of δt*. The weight is the inverse of the expected standard deviation of δt* due to random noise (Appendix 1.2). Symbols are placed at station locations. Larger symbols indicate greater δt*.

attenuation decreases with increasing frequency.

4.1 Effects of Composition

The relationships between the shear attenuation model and shear velocity model are presented in Figure 8. The relative shear velocity model is converted to absolute velocities by assuming the values given by Lee and Grand [1996] are relative to PREM and that the average shear velocities in the model below 250 km depth are equal to PREM. To make this comparison and perform the analysis below, we must also assume that the frequencies used to measure velocity and attenuation are the same, ~0.6 Hz.

Compositional and thermal effects can result in a given value of attenuation and velocity. If we assume that Q has a positive power law dependence with respect to frequency ($\alpha > 0$), Minster and Anderson [1981] provide the following relationship between velocity and attenuation

$$V_S(w) \approx V_U\left[1 - \frac{1}{2}\cot\frac{\alpha\pi}{2} Q_S^{-1}(w)\right]. \qquad (14)$$

V_U is the unrelaxed shear velocity due either to sufficiently high frequency or low temperature where anelastic mechanisms do not have time or energy to operate. The unrelaxed velocity depends primarily on composition. For example, the fractional change in the unrelaxed shear velocity relative to the fractional change in the iron content for Proterozoic sub continental lithospheric mantle (SCLM) [*Griffin et al.*, 1999], $\partial \ln V_S / \partial X_{Fe}$, is approximately -0.3 (Table 4). A 1% decrease in iron content increases the shear velocity by 0.3%. Decreasing iron content, an effect that accompanies older and more mature SCLM and the melting

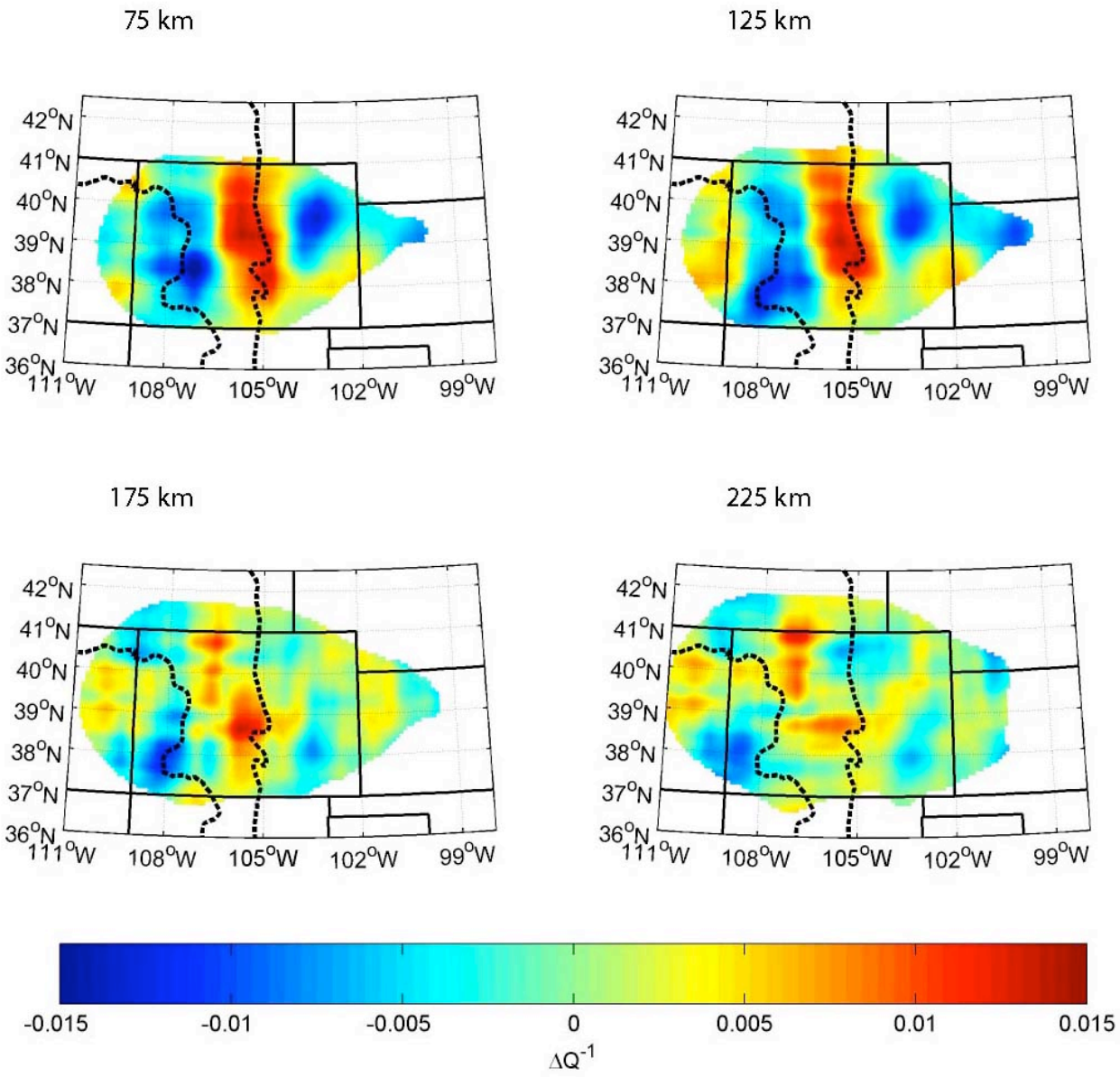

Figure 7. Differential attenuation tomography results at four depths. Relatively strong attenuation occurs beneath the eastern Rocky Mountains to depths of ~150 km and trends north from the Rio Grande Rift.

of mantle peridotite, increases the seismic velocity. Another compositional effect that can change shear velocity is simply the bulk mineralogy. More mature SCLM typically has less garnet and more olivine. In going from the Phanerozoic to Archean compositions reported by Griffin et al. [1999] where garnet decreases by 4% and olivine increases by 3%, shear velocity increases by 5%.

If the relationship provided by Minster and Anderson is correct and we know α, then we can use velocity and attenuation models to solve for changes in V_U, an indicator of compositional variation. Values for _ measured in the laboratory on polycrystalline aggregates under upper mantle conditions at seismic frequencies range from 0.2 to 0.3 [Karato and Spetzler, 1990]. Seismological estimates for α are on the order of 0.15 [Warren and Shearer, 2000; Sobolev et al., 1996].

The straight lines in Figure 8 represent different values of α in equation 14. For the upper layers at 75 and 125 km depth, the overall trend in the data shows low values of α, on the order of 0.15. If we examine the slope of the smaller scale trends and trends at greater depth, 175 and 225 km, we see that the slope increases to values of α closer to 0.25. We therefore examine compositional variability by rearranging equation 14, using the V_S and Q^{-1} models and assuming α equals 0.25, and solving for the percent change in unrelaxed shear velocity, $\%\Delta V_U$. The resulting compositional models presented below do not change significantly for α equal to 0.15.

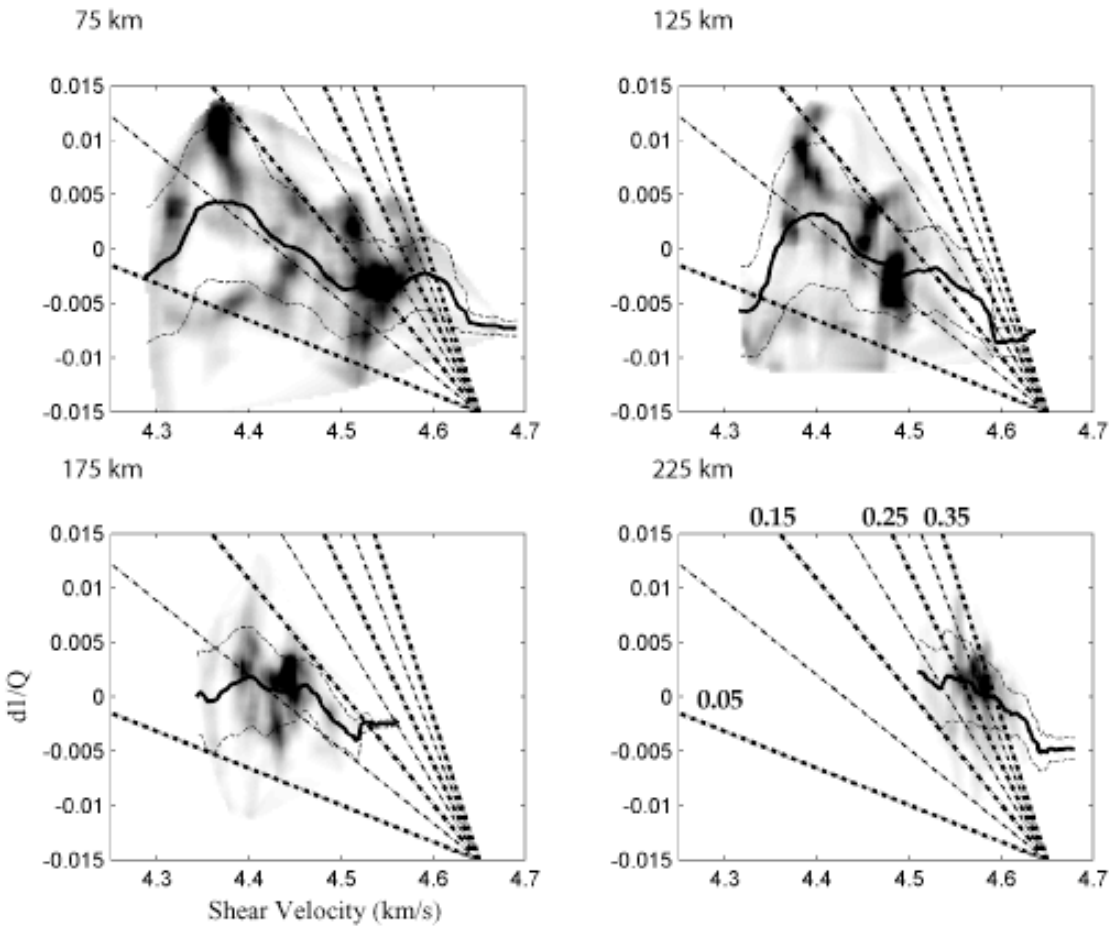

Figure 8. Velocity versus relative attenuation for four depths. The gray scale is proportional to the number of model points having that velocity and attenuation, a 2-D histogram. The dashed-dot lines are plots of velocity versus attenuation according to equation 14 for different values of _. Movement along a line is due to changing temperature while movement across a line is due to changing V_U or composition. Seismological studies have found _ equal to 0.15 [*Warren and Shearer*, 2000; *Sobolev et al.*, 1996] while laboratory experiments have found _ between 0.2 and 0.3 [*Karato and Spetzler*, 1990].

Figure 9 contains horizontal slices of the relative unrelaxed shear velocity. Unrelaxed shear velocities tend to increase gradually to the east and may reflect temperature dependent phase changes such as the reactions in Table 4. Application of equation 14 predicts very low unrelaxed shear velocities beneath the southwestern Colorado Rocky Mountains. If this were partial melt and the local fluid flow attenuation mechanism were operating [*Hammond and Humphreys*, 2000b; *Hammond and Humphreys*, 2000a], we would see relatively low unrelaxed velocities. A shear velocity reduction of 6.5% would indicate 0.8% partial melt (Table 4). But conventional models of attenuation in which attenuation simply increases with temperature suggest that attenuation would remain high since high temperatures would presumably be needed to produce partial melt. Since the shear wave attenuation has dropped considerably, we have either observed a very unusual composition or the high temperature side of an attenuation peak [*Anderson and Given*, 1982]. If we are in fact on the high temperature side of an attenuation peak, equation 14 no longer holds in this region and unrelaxed velocities are greater than presented in Figure 9. After assessing the possible changes in temperature, we will return to the question of composition.

4.2 Effects of Temperature

We can calculate changes in temperature for the case of either unusual composition or the high temperature side of an attenuation peak. We adopt the relation for the temperature derivative with respect to shear velocity given by Karato [1993] including effects of pressure,

$$\frac{\partial \ln V_S(\omega)}{\partial T} = \frac{\partial \ln V_U}{\partial T} - F(\alpha)\frac{Q^{-1}(\omega)}{\pi}\frac{H^* + PV^*}{RT^2}. \quad (15)$$

$\partial \ln V_U/\partial T$ is the normalized derivative of the shear velocity with respect to temperature for the unrelaxed state. From 50 to 400 km depth, $\partial \ln V_U/\partial T$ for olivine, assumed to be the dominant mineral in the upper mantle for this region, is approximately -0.76 x 10^{-4} K^{-1} [*Karato*, 1993]. ω is the angular frequency. $F(\alpha)$ is a constant related to the

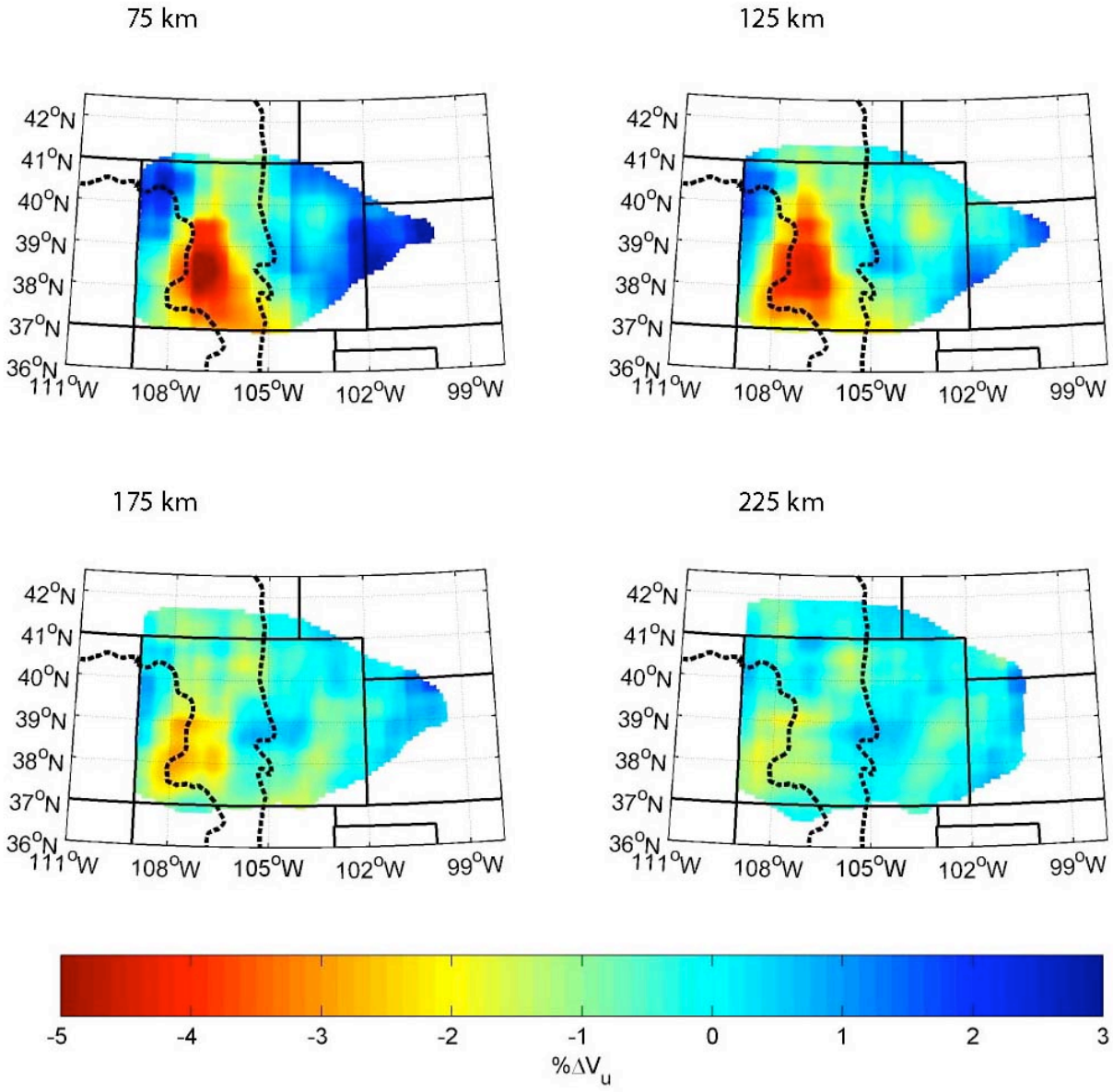

Figure 9. Unrelaxed shear velocity at four depths. Unrelaxed shear velocity gradually increases to the east from the Colorado Rockies. A significant drop in unrelaxed shear velocity occurs beneath the southwest Colorado Rocky Mountains and may indicate either high temperatures and an attenuation peak or unusual compositions.

frequency dependence of attenuation where Q is proportional to ω^{α}. $F(\alpha)$ is given by

$$F(\alpha) = \frac{\pi\alpha}{2}\cot\frac{\pi\alpha}{2}. \qquad (16)$$

Again we choose $\alpha = 0.25$ which gives $F(\alpha) = 0.95$. As α goes to 0, $F(\alpha)$ goes to 1. A larger value of α reduces the dependence of (15) on Q. H^* is the activation energy of the thermally activated process, V^* is the activation volume, P is the pressure, R is the gas constant and T is the reference temperature. We use $H^* = 500$ kJ/mol, the activation energy for the diffusion of oxygen through olivine [*Karato and Spetzler*, 1990]. The activation volume, V^*, controls how pressure affects the activation energy. We use $V^* = 4 \times 10^{-6}$ m^3/mol [*Anderson*, 1989]. The pressure in the mantle is taken from PREM [*Dziewonski and Anderson*, 1981] and the reference temperature is taken from the geotherm reported by Stacey [1992], ~1200 to 1800 K from 50 to 400 km depth.

This formulation requires absolute attenuation. In addition, to account for composition, we must consider $\partial \ln V_S$ for velocities relative to the unrelaxed shear velocity, $(V_S - V_U)/V_U$, for which the calculation of V_U also requires absolute attenuation. We determine absolute attenuation by assuming that the smallest absolute attenuation in our model is close to zero and add a constant value to our differential attenuation model. We add 0.015 to our relative attenuation model and require attenuation to be positive and greater than 0.005. The requirement that absolute

attenuation be greater than 0.005 is done only to inhibit extreme changes in temperature.

We must now consider two cases when applying (15) to derive changes in temperature. The first case assumes that the power-law relation between velocity and attenuation, equation 14, holds in all regions and that the composition of the upper mantle beneath the southwest Colorado Rocky Mountains is unusual. In this case, changes in temperature derived from equation 15 are independent of velocity since the fractional change in velocity becomes only a function of attenuation,

$$\partial \ln V_S = -\frac{1}{2}\cot\frac{\alpha\pi}{2} Q_S^{-1}. \qquad (16)$$

Changes in temperature are then proportional to attenuation with the greatest increase in temperature beneath the eastern Colorado Rocky Mountains (Figure 10a). At 125 km depth, temperatures are elevated to about 80 K greater than the anomalous region to the southwest and only 50 K greater than the Great Plains. For the second case, where the anomalous region is due to an attenuation peak, the unrelaxed shear velocity is not allowed to fall below the highest unrelaxed shear velocity along the boundaries of this anomalous region. Equation 15 for velocity-temperature relations still holds, though for a different value of α as it goes to zero and becomes negative on the high temperature side of the attenuation peak. We continue to use α equals 0.25 and incur a small penalty. For this case, temperatures at 125 km depth beneath the southwest Colorado Rocky Mountains increase by over 300 K (Figure 10b).

4.3 Upper Mantle Composition and Isostatic Compensation

An additional constraint to help us differentiate the possible thermal and compositional models is the subsurface density distribution required to support the Rocky Mountains and surrounding regions. We first account for thermal contributions to upper mantle isostacy for the two temperature models and isostatic compensation due to thickened crust [*Li et al.*, 2002] assuming a constant density contrast across the Moho of 400 kg/m^3. We then look for the relationship between density and velocity in the upper mantle that produces the best variance reduction of the residual topography. This relationship is compared to predicted values to estimate the compositional heterogeneity in the upper mantle. The remaining topography, after accounting for the above factors, is due to density anomalies in the crust.

Fractional changes of density with respect to velocity, $\partial\ln\rho/\partial\ln V_S$, are estimated for several different mineral reactions, changes in temperature, and partial melt (Table 4). Density, velocity and thermal expansivity (~ 3.3×10^{-5} K^{-1}) are calculated using the techniques of Bina and Helffrich [1992] and Holland and Powell [1998] and the mineral data compiled by Hacker et al. [2003]. A starting mineral assemblage of preferred Proterozoic SCLM [*Griffin et al.*, 1999] is used and the above values are averaged from 50 to 200 km depth. We compute the mantle thermal component of isostatic compensation using the two differential temperature models described previously while assuming that mass anomalies affecting compensation are confined to between 50 and 200 km depth. The mass needed to compensate the mass deficit in the mantle results in topography having a density of 2700 kg/m^3 [*Snelson et al.*, 1998]. We also calculate the crustal component of isostatic compensation using the crustal thickness map of Li et al. [2002] and a density contrast across the Moho of 400 kg/m^3.

Figure 11 shows the variance reduction of smoothed topography in dependence on $\partial\ln\rho/\partial\ln V_S$ for the upper mantle due to changes in composition while accounting for upper mantle thermal and crustal thickness contributions. Thickened crust alone accounts for 57% of the topographic variance (solid horizontal line). Up to an additional 7% of the variance can be explained by the thermal variations in the upper mantle (short horizontal lines spanning their associated values of $\partial\ln\rho/\partial\ln V_S$). Two cases are presented representing the two possible relationships between velocity and attenuation. Each case results in a thermal model and compositional model. The dashed-dot line represents mantle contributions to isostacy when there is an attenuation peak (case 1) while the dashed line represents contributions when attenuation has a simple linear relationship to velocity (case 2). The vertical lines are values of $\partial\ln\rho/\partial\ln V_S$ for the different compositional effects in Table 4. For case 1 where high temperatures coincide with the lowest shear velocities, the thermal model increases the variance reduction by 7%. The compositional counterpart for this case adds little improvement. For case 2 where unusual composition coincides with the lowest shear velocities, the thermal model increases the variance reduction by less than 1% but the corresponding compositional model improves the variance reduction by 14%.

For both relationships between velocity and attenuation, the best $\partial\ln\rho/\partial\ln V_S$ lies somewhere between melt with basalt depletion and the other mineral reactions. Assuming that no Fe/Mg fractionation occurs for reactions 1-6 (Table 4), the measured value of $\partial\ln\rho/\partial\ln V_S$ implies that some melt is present. The high temperature case would make hydrous phases unstable. Antigorite is stable below 1000 K [*Bromiley and Pawley*, 2003] while phlogopite can remain stable up to 1600 K [*Sato et al.*, 1997]. Increasing temperature is likely to drive garnet to orthopyroxene and corundum (reaction 2) [*Aranovich and Berman*, 1997] or garnet and olivine to orthopyroxene and spinel (reaction 6) [*Danckwerth and Newton*, 1978]. These reactions have the correct sense in that higher temperatures produce compositions that are slower and lighter, however reaction 2 is unlikely to produce a large signal because of its small values of $\partial\ln V_S/\partial R$ (Table 4) and $\partial R/\partial T$ [*Aranovich and Berman*, 1997]. Though the high temperature model with

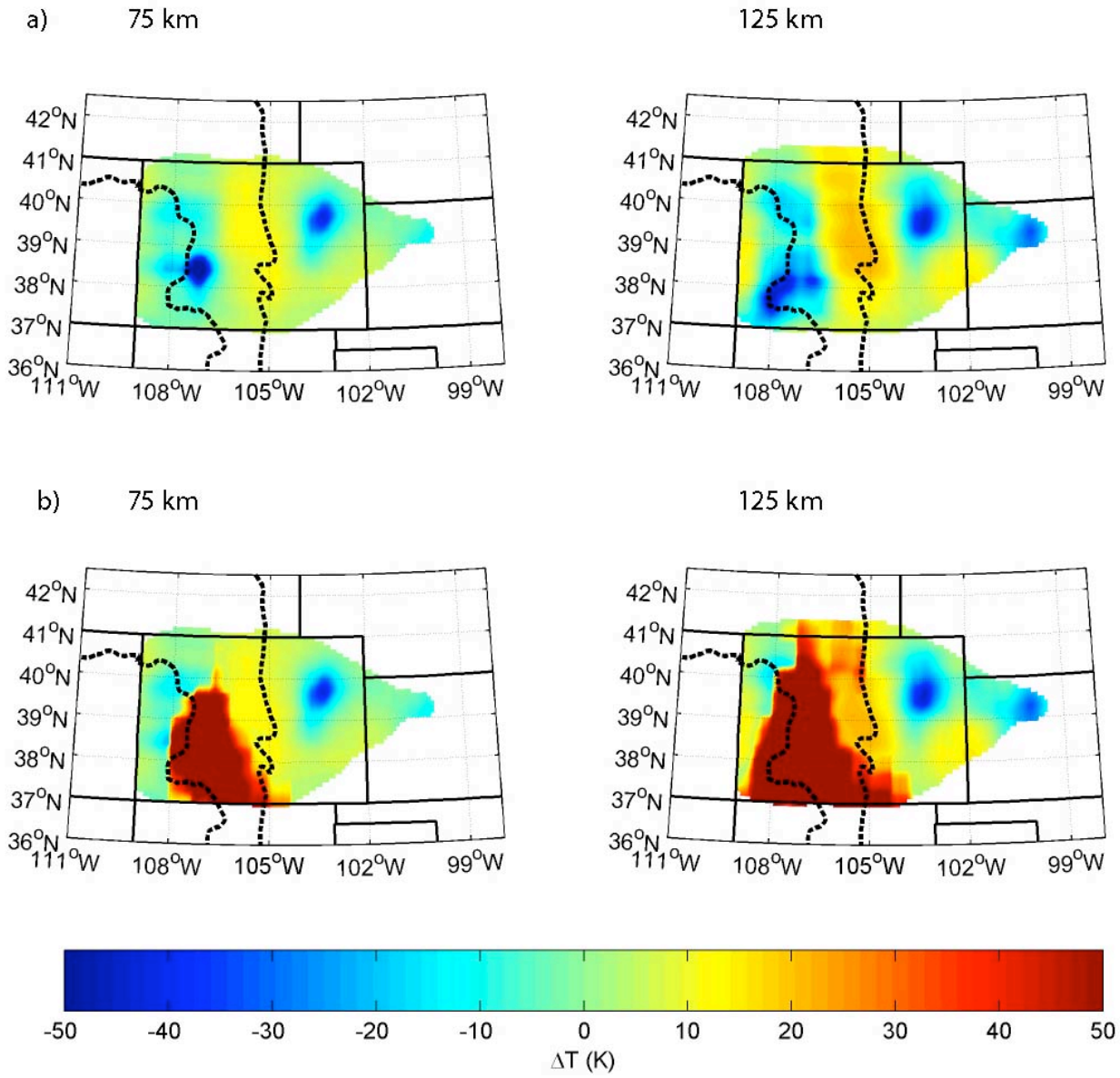

Figure 10. Temperature contrast at 75 and 125 km depth from the use of equation 15. In a) equation 14 holds in all regions, i.e. there is no attenuation peak. Maximum temperature contrasts are limited to elevated values of 80 K at 125 km beneath the eastern Colorado Rockies. In b) equation 14 holds everywhere except in the region of very low unrelaxed shear velocity, i.e. the low velocities beneath southwest Colorado are due to an attenuation peak resulting from very high temperatures. Unrelaxed shear velocity is not allowed to drop below the values on the edge of the anomalously slow region, -2%_V_U. Maximum temperature contrasts increase to elevated values of over 300 K at 75 km beneath the southwestern Colorado Rockies.

its' associated compositional variations produces a consistent interpretation, the second case in which velocity has a simple linear relationship with respect to attenuation produces a better variance reduction. For such a model, elevated temperatures are slight and melt will only be present if the melting temperature has been reduced by the presence of hydrous phases. Antigorite is unlikely to be stable very far below the Moho while phlogopite could be stable throughout most of the mantle lithosphere. The presence of phlogopite in the upper mantle beneath southwest Colorado is consistent with its presence in lamproite dikes in the Colorado Plateau [*Wannamaker et al.*, 2000] and highly potassic magmatism in southwest Colorado [*Mutschler et al.*, 1987].

Researchers have speculated on the presence of phlogopite in the upper mantle beneath southwest Colorado but have not been able to determine its subsurface extent. If we assume that our data is explained by the presence of phlogopite and partial melt, we can derive their proportions from the estimated $\partial \ln\rho / \partial \ln V_S$ in Figure 11, 0.096, and the relations

$$\partial \ln \rho = \{\partial \ln \rho\}_A + \{\partial \ln \rho\}_B \qquad (17)$$

Table 4. Density – Velocity Relationships

R	$\frac{\partial \ln \rho}{\partial \ln V_S}$	$\frac{\partial \ln \rho}{\partial \ln V_P}$	$\frac{\partial \ln V_S}{\partial R}$	$\frac{\partial \ln V_P}{\partial R}$	$\frac{\partial \ln V_S}{\partial \ln V_P}$
1	-0.98	-1.58	0.27	0.17	1.6
2	0.66	0.46	-0.01	0.02	0.7
3	0.38	0.46	-0.07	-0.06	1.2
4	0.30	0.40	-0.63	-0.47	1.3
5	0.31	0.58	-0.92	-0.48	1.9
6	0.86	0.57	0.10	0.14	0.7
7	0.14 to 0.43	0.15 to 0.53	-2.32×10^{-4} to -0.76×10^{-4}	-2.18×10^{-4} to -0.62×10^{-4}	1.1 to 1.2
8	0.03	0.06	-7.90	-3.60	2.2
9	-0.01	-0.02			2.8

Table 4. Density-velocity relationships for various conditions corresponding to a pressure of 3 GPa and temperature of 1240 K or ~ 100 km depth. R is the reaction number corresponding to the following scenarios: 1. Increasing Mg# (Mg/(Mg + Fe)) [*Griffin et al.*, 1999], 2. Increasing garnet at the expense of orthopyroxene and corundum [*Aranovich and Berman*, 1997], 3. Increasing phlogopite at the expense of garnet (above 4.5 GPa) [*Sato et al.*, 1997], 4. Increasing phlogopite at the expense of olivine (below 4.5 GPa) [*Sato et al.*, 1997], 5. Increasing antigorite at the expense of olivine [*Bromiley and Pawley*, 2003], 6. Formation of olivine and garnet at the expense of orthopyroxene and spinel [*Danckwerth and Newton*, 1978], ∂R expressed as an increase in the fraction of olivine, 7. Rising temperature where the upper number results from a quality factor of 50 and the lower number results from an infinite quality factor [*Karato*, 1993], 8. Increasing partial melt [*Hammond and Humphreys*, 2000b], and 9. Increasing partial melt with depletion of iron [*Humphreys and Dueker*, 1994]. ∂R is the fractional increase of the appropriate mineral (R 1-6), change in temperature (R 7) having units of K, or fractional increase in partial melt. For reactions 1-6, values were obtained using the method of Bina and Helffrich [1992] and Holland and Powell [1998] and the mineralogical data of Hacker et al. [2003]. Values for reaction 7, changes in temperature, were obtained from Karato [1993]. Values for melt were obtained from Hammond and Humphries[2000b] assuming $\partial \ln\rho/\partial R$ is -0.2 [*Humphreys and Dueker*, 1994] and the following relationship for melt with depletion of iron in the residuum

$$\frac{\partial \ln \rho}{\partial \ln V} = \frac{A\left\{\partial \ln \rho / \partial \ln V\right\}_\alpha + \left\{\partial \ln \rho / \partial \ln V\right\}_\beta}{A+1}$$

where α represents values for melt and β represents values for depletion of iron. A is equal to

$$A = \frac{\left\{\partial \ln V / \partial R\right\}_\alpha}{\left\{\partial \ln V / \partial R\right\}_\beta}.$$

$$\partial \ln V_S = \left\{\partial \ln V_S\right\}_A + \left\{\partial \ln V_S\right\}_B \qquad (18)$$

which give

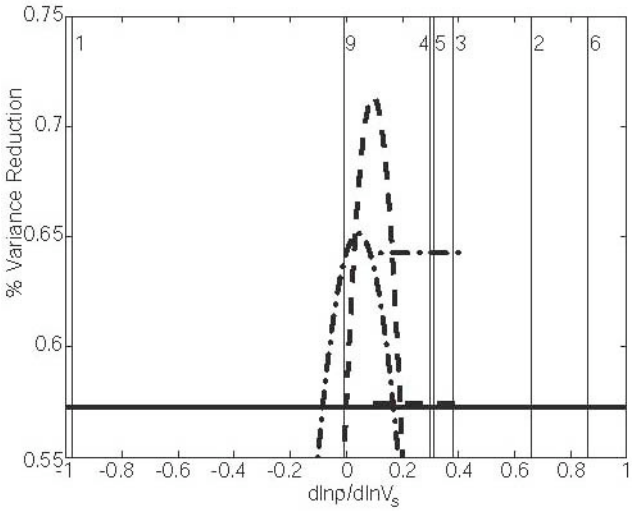

Figure 11. Variance reduction of elevation data versus fractional derivative of density with respect to shear velocity. The solid horizontal line is the variance reduction for thickened crust. The dashed line represents the low temperature model while the dashed-dot line represents the high temperature model. The short horizontal lines indicate the variance reduction due to the addition of thermal effects and span the appropriate range of $\partial \ln\rho/\partial \ln V_S$ for that phenomenon. The curved lines represent the addition of the compositional component of mantle compensation for a range of $\partial \ln\rho/\partial \ln V_S$. The vertical lines are values of $\partial \ln\rho/\partial \ln V_S$ for the different compositional effects in Table 4.

$$\frac{\partial \ln \rho}{\partial \ln V_S} = \left\{\frac{\partial \ln \rho}{\partial \ln V_S}\right\}_A \frac{\left\{\partial \ln V_S\right\}_A}{\partial \ln V_S} + \left\{\frac{\partial \ln \rho}{\partial \ln V_S}\right\}_B \frac{\partial \ln V_S - \left\{\partial \ln V_S\right\}_A}{\partial \ln V_S}. \qquad (19)$$

The subscript A denotes reaction 9, melt with depletion, and subscript B denotes reaction 4, substitution of olivine with phlogopite. In solving for $\{\partial \ln V_S\}_A/\partial \ln V_S$, the fraction of velocity anomaly due to partial melt, we find that 66% of the velocity anomaly is due to melt and the remainder, 34%, to phlogopite. Using the derivatives of velocity versus phlogopite or melt fraction (Table 4) and the fractional change in the unrelaxed velocity, we conclude that if up to 6% of the unrelaxed velocity anomaly is due to these processes, there is up to 0.5% partial melt and up to 3% substitution of olivine with phlogopite beneath the southwest Colorado Rockies. If the unrelaxed shear velocities beneath southwest Colorado were higher due either to greater anelastic shear velocities or greater attenuation, the value of $\partial \ln\rho/\partial \ln V_S$ for which there is a maximum variance reduction of residual topography would be greater. Because of this and the reduction in the velocity anomaly, there would be less partial melt.

The residual elevation anomaly after accounting for thickened crust and the thermal effects of the low

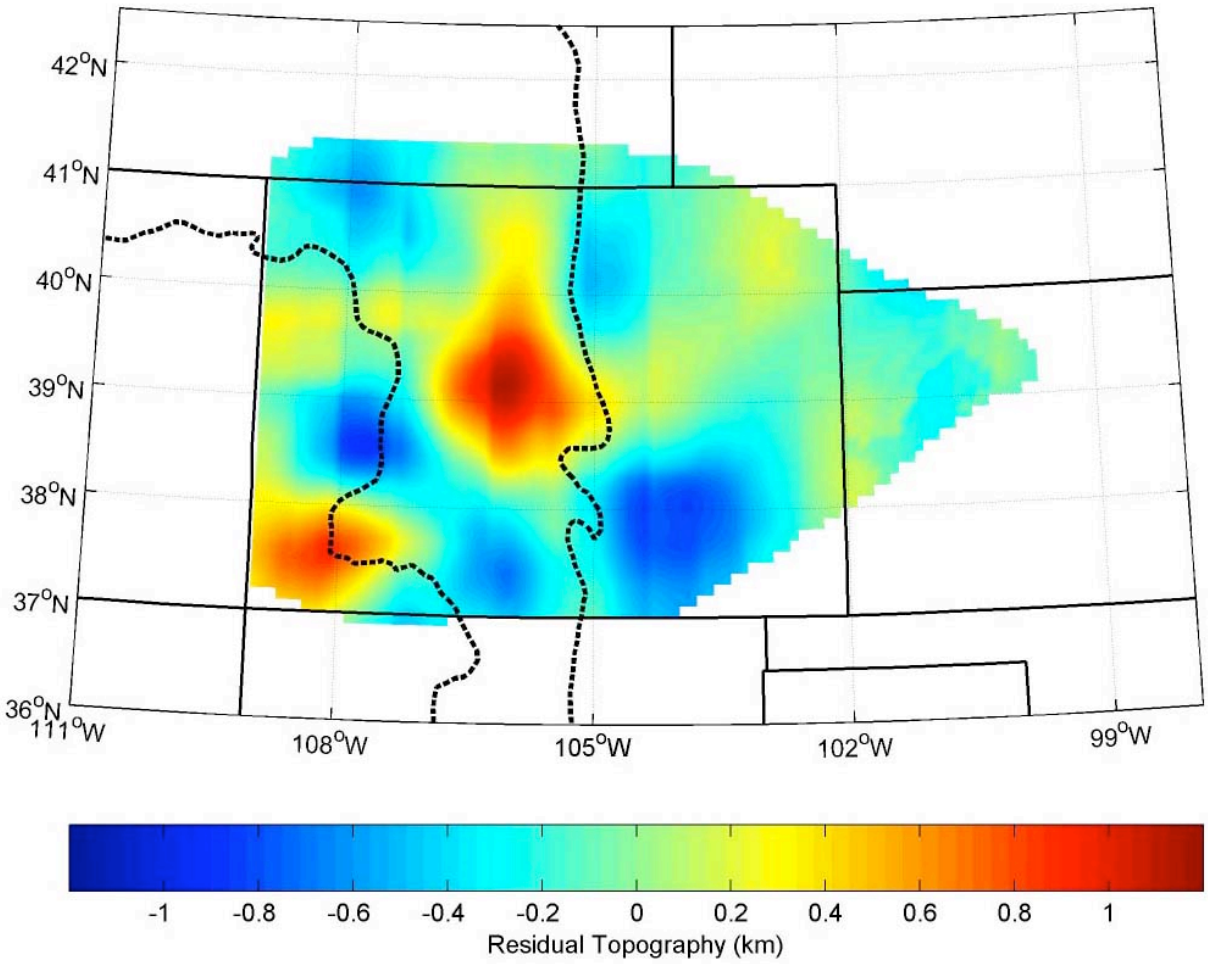

Figure 12. Residual topography after the compensation of thickened crust and upper mantle density contrasts. The remaining uncompensated topography is in the central Colorado Rockies, a position coinciding with low crustal shear velocities and the inferred presence of a large low density granitic intrusion.

temperature upper mantle model and its associated compositional effects as stated in the previous paragraph is shown in Figure 12. Nearly 1.5 km of elevation remains in central Colorado. Work by Li et al. [2002] have found slow shear wave velocities in the crust of central Colorado and attributed these slow velocities to low density granitic intrusions [*Decker et al.*, 1988]. To account for the residual elevations in central Colorado, the density of this material distributed over the full height of the crust, 45 km, should be reduced by about 3%. Decker et al. suggested 4.5% but distributed the anomaly over 30 km of the upper crust.

Some of the negative elevation residual anomalies coincide with the thickest crust (e.g. southwest Colorado). Li et al. point out that their crustal thickness model would allow a 5 km reduction in crustal thickness to be compensated by a 3% reduction in shear velocity. If limited to the negative anomalies in the southwest Colorado Rocky Mountains, this effect would reduce the variance of the elevation residual and provide a better correlation between the velocity models of Li et al. [2002] and that of Lee and Grand [1996].

5. CONCLUSION

Before too much weight is given to any interpretation, we must respect the amount of uncertainty. The primary problem with the results presented above and most field t^* measurements is the significant amount of noise expected for each measurement. Appendix 1 sheds light on some of the possible errors present in the δt^* measurement while Appendix 2 evaluates the effect of some of this error on model resolution. Errors considered for the δt^* measurement include normally distributed random noise and non random noise from basin reflections. Additional errors that are not considered include anisotropy, multipathing, improper ray tracing resulting from not using a three dimensional velocity model and frequency dependent variations in amplitudes across the array resulting from source radiation patterns. In addition to the uncertainty of the observations, the theoretical relationship between shear velocity and attenuation is uncertain. Rock physics experimentation has made progress but has had difficulty making absorption and dispersion measurements

under mantle conditions at seismic frequencies with rocks of appropriate composition. Further, the temperature models presented above are relative and knowing the correct phase relationships between mineral assemblages requires knowing the absolute pressure and temperature.

Aside from the uncertainties, several results can be stated. High attenuation underlies the eastern Colorado Rockies and is likely due to elevated temperatures. East of the Rockies, attenuation gradually decreases as velocity gradually increases reflecting at least a simple decrease in temperature. To the west low attenuation coincides with the lowest velocities, and the interpretation is less conclusive. If a frequency limited attenuation band is active, the low velocities and low attenuation may be very hot mantle, over 300 K above its surroundings. If attenuation obeys a more simple relationship to velocity as in equation 14, this anomalous region is due to compositional variation. Our preferred model assumes a linear relationship between velocity and attenuation over the temperatures and frequencies encountered in this study and suggests that the southwest Colorado Rockies are underlain by up to 0.5% partial melt and the substitution of up to 3% olivine with phlogopite.

After the addition of various density anomalies, we find that the Colorado Rocky Mountains are supported by low density mantle, thick crust [*Li et al.*, 2002], and in some cases, low density crust [*Li et al.*, 2002]. The low density mantle may either be thermal and/or compositional in origin. The presence of recent and potassic magmatism above the anomalous region suggests that partial melt and the presence of phlogopite are responsible for at least some of the decrease in velocity and density.

APPENDIX 1. SOURCES OF ERROR

A1.1. Errors due to non Random Noise and the Sedimentary Basin Correction

Interference produced by non random noise, specifically a set of reflections from the bottom of a sedimentary basin, can lead to significant apparent δt^*. Though the only source accounted for in this study, this type of error can also be caused by shear wave splitting, S to P conversions, and focusing/defocusing. The contribution to δt^* from this effect can produce larger values than those due to a highly attenuating upper mantle. Contributions to δt^* from intrinsic attenuation in the basin are negligible since the travel time through the sediments is small. For example, a seismic wave traveling through a 4 km thick basin with a shear velocity of 2 km/s will spend 2 seconds in the basin. If the basin has a Q of 50, t^* will be 0.04, an order of magnitude smaller that the correction due to basin reflections. In this section, different reflectivity series corresponding to a range in arrival times of the first reflector are convolved with the event waveforms in Figure A1.1, event #405 and event #412, and apparent δt^* is

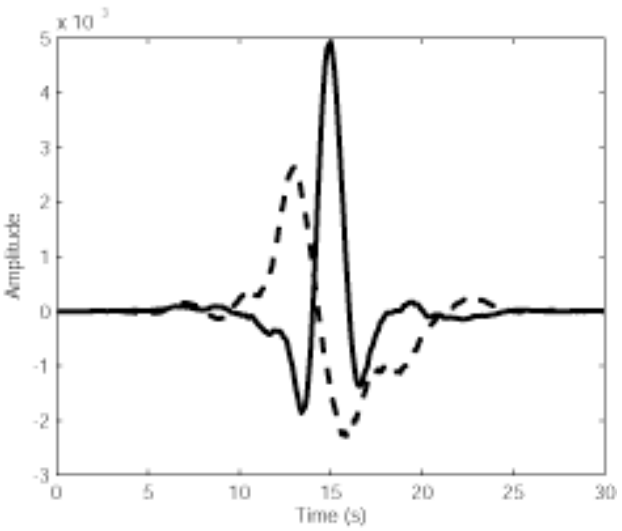

Figure A1.1. Two reference signals where the reference signal is the aligned stack of all S-waves for a given event. The dashed curve is Event #405 and the solid curve is Event #412.

calculated for the reverberating time series relative to the original.

Figure A1.2 shows the apparent δt^* for the two example event waveforms in Figure A1.1 in dependence on the time of the first reflected arrival. The curves represent a case with a normal incident reflection coefficient of -0.3, a typical value expected for the bottom of a sedimentary basin. For a 4 km thick basin with a shear velocity of 2 km/s, a possible scenario for the stations in the Denver Basin, the first reflected arrival will lag the direct arrival by 4 seconds. Depending on the event shape, apparent δt^* could be about -0.5 seconds.

The functional relationship between δt^* error and time lag between the direct arrival and the reflected waves depends on the temporal shape and extent of the event pulse, the relative size between the direct arrival and the reflection, and the frequency range over which the δt^* measurement is made. Apparent δt^* due to basin reflections is calculated for all stations sitting on known sedimentary basins. A synthesized reflectivity sequence is convolved with each event pulse. The reflectivity sequence is generated using basin thicknesses reported by Sheehan et al. [1995] and Burchfiel [1992] and rock densities and P-wave velocities estimated for the crust and basins of Colorado by Snelson et al. [1998] and Prodehl and Lipman [1989]. To obtain shear wave velocities, we assume V_p/V_s of 1.75 in the crust and 2.0 in the basins [*Sheehan et al.*, 1995; *Catchings*, 1999; *Hauksson*, 2000; *Ludwig et al.*, 1970; *Christensen*, 1996]. The value for the basin V_p/V_s ratio was determined by maximizing the δt^* variance reduction for different values of basin V_p/V_s ratio. The variance reduction of δt^* for the Q^{-1} tomography due solely to basin reflections is 11%. The mean δt^* correction is -0.11, the maximum, 0.05, and minimum, -0.86. Specific values for the corrections are listed in Table 3.

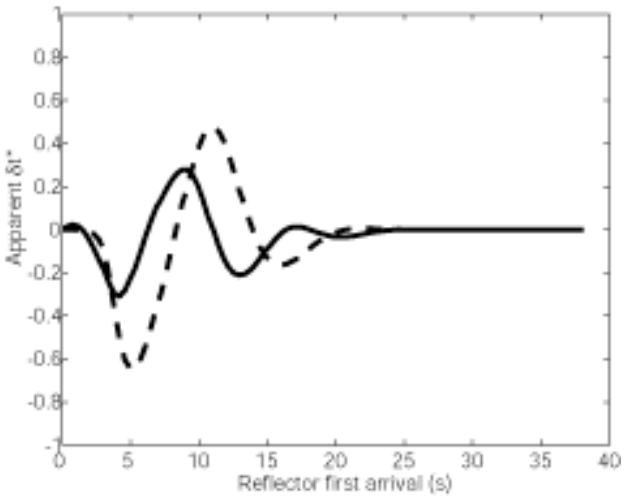

Figure A1.2. Apparent δt^* versus time of arrival for the first reflector due to a normal incident reflection coefficient of -0.3. The results are for the signals in Figure A1.1 (dashed curve – Event #405, solid curve – Event #412). For long offsets, the reflection is no longer in the window of interest and apparent δt^* goes to zero. At shorter offsets, apparent δt^* oscillates at different rates depending on the frequencies with which δt^* is measured and the shape of the source time series. The range in time of arrival for the first reflector from the bottom of sedimentary basins in this study is 0.5 to 5.2 seconds. Reflections from the bottom of the crust would come in around 25 seconds.

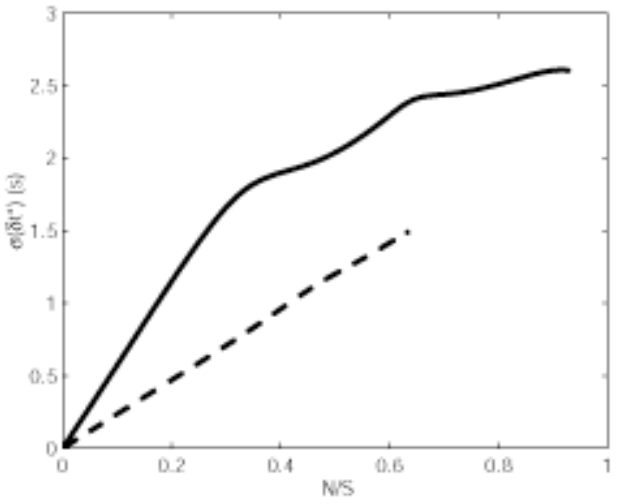

Figure A1.3. The sensitivity of the reference signals in Figure A1.1 to random noise (dashed curve – Event #405, solid curve – Event #412). These two signals produce extremes in sensitivity, the slope between the standard deviation of δt^* and the noise to signal ratio (Table 2).

A1.2. Errors due to Random Noise.

Our next goal is to determine the effect of random temporal noise on the measurement of δt^*. Two reference time series, event #405 and event #412 (Figure A1.1), which represent extremes in sensitivity to temporal noise are contaminated in the time domain with varying levels of normally distributed random noise. For each level of noise, a noise vector is generated and multiplied by a gaussian taper, added to the signal and the signal to noise ratio and δt^* are measured. The signal to noise ratio is measured as described in Section 2 except that the noise spectrum is calculated from the tapered noise vector. δt^* is measured as in Section 2 and measured relative to the clean signal. The process is repeated 1000 times for each noise level to derive the standard deviation of δt^* due to that level of normally distributed random noise.

Figure A1.3 shows the effect of noise on the example reference time series where the standard deviation of δt^* is plotted versus the noise to signal ratio. As the noise to signal ratio increases, the standard deviation of δt^* increases approaching values of 2.5 seconds. The relationship between the standard deviation of δt^* and noise to signal ratio is approximately linear for small to moderate values of the noise to signal ratio and for most of the δt^* data used in the Q^{-1} tomography study. We assume that the noise in our signals for this study can be described by a normally distributed random process and use the slopes of standard deviation of δt^* versus the noise to signal ratio derived from Figure A1.3 (Table 2) for each event and the signal to noise ratios for each signal (Table 3) to derive the standard deviation of δt^* for each measurement. The inverse of these values are applied as weights in the inversion. This analysis leads to the conclusion that 75% of the variance of δt^* for this study, after accounting for basin reflections, is due to normally distributed random noise.

APPENDIX 2: MODEL RESOLUTION

Typically the resolution matrix will give you an estimate of the uniqueness of a solution based only on the ray path geometry, $d\tau^{-1}$. The resolution matrix, R, is defined

$$R = M_p M_p^T \qquad \text{(A2.1)}$$

where M_p is the matrix of eigenvectors defined in (11). Figure A2.1 shows that the resolution across most of the Colorado Rocky Mountains is near 1.0. The resolution matrix, however, does not account for uncertainty in the observations. To assess the effect of uncertainty in δt^* on the resolution of the solution, we use checkerboard tests.

The checkerboard model is composed of 200 × 200 × 400 km blocks having an attenuation, ΔQ^{-1}, of either +0.03 or -0.03. Observations are produced according to equation 9, and the inversion is performed as outlined in Section 3. One can take the synthetic observations and re-invert for the model to estimate model resolution (Figure A2.2). An inspection of Figure A2.2 shows that the ray geometry provides good resolution. Areas within the model remain well resolved while areas along the edges of the model

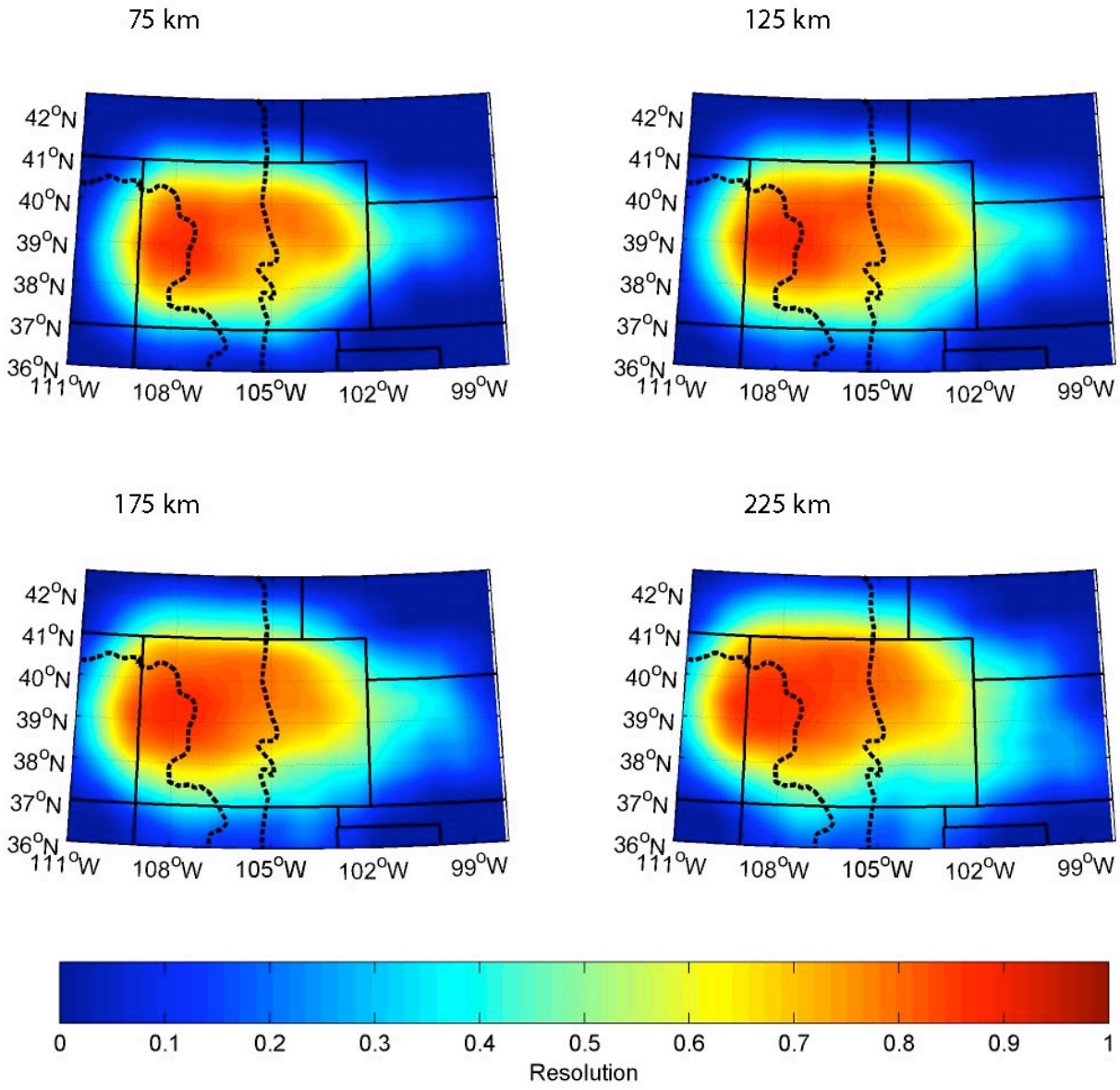

Figure A2.1. Resolution matrix showing model resolution at four depths. The resolution increases to near one throughout most of the upper mantle beneath Colorado.

space become distorted. The true resolution, however, can only be considered when errors are introduced to the observations [*Tarantola*, 1987]. The problem is estimating the proper amount of error to add to the observations.

In Appendix 1.1, we found that based on our data's signal to noise ratios and the shape of the reference time series, normally distributed random noise accounts for 75% of the δt^* data variance. A random value scaled by a constant multiplied by the standard deviation of δt^* is added to the checkerboard data. The constant is determined by requiring that 75% of the checkerboard data variance is due to random error, the same condition that is present in the real data. The standard deviation of δt^* is also used as the inverse of the weight in the inversion. It is found by dividing the data's signal to noise ratio (Table 3) by the slope of the standard deviation of apparent δt^* versus the synthetic noise to signal ratio (Section 1.2; Table 2). Now having some idea of the error in the observations and how to weight the inversion, we can interpret a more representative checkerboard test to assess model resolution (Figure A2.3). The inverted checkerboard model is only slightly more distorted than the inversion without error. The amplitude of variations between checkers is amplified which helps to counteract the effect of damped intrinsic δt^* values from the tapering processes. The checkerboard results suggest that a properly weighted inversion, even with the amount of random error expected for our data set, can still produce reasonable results.

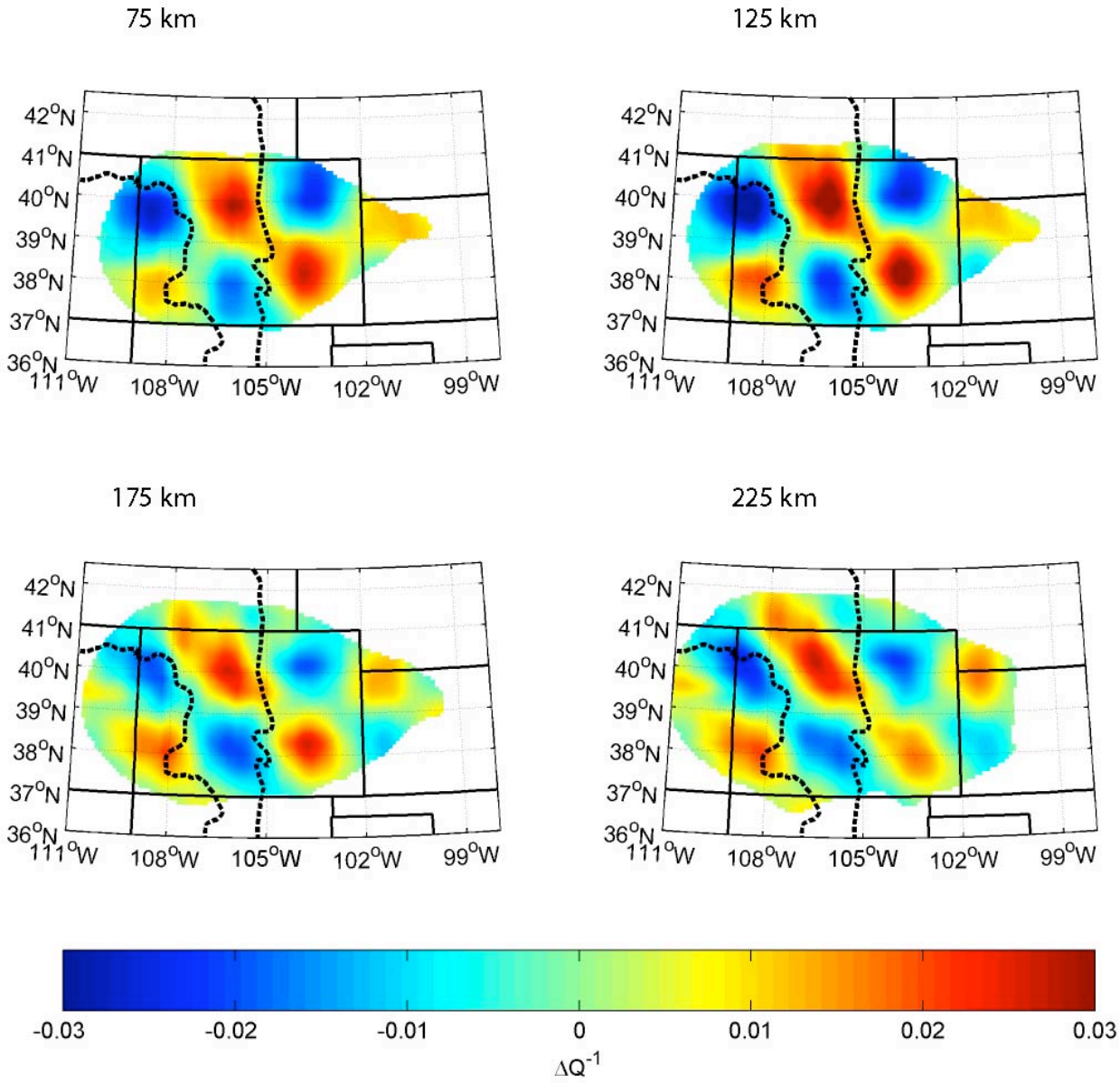

Figure A2.2. Checkerboard results for observations without error at four depths. Input model consists of 200 × 200 × 400 km blocks of alternating attenuation, +0.03 and -0.03. The checkerboard remains fairly well resolved where the resolution is high.

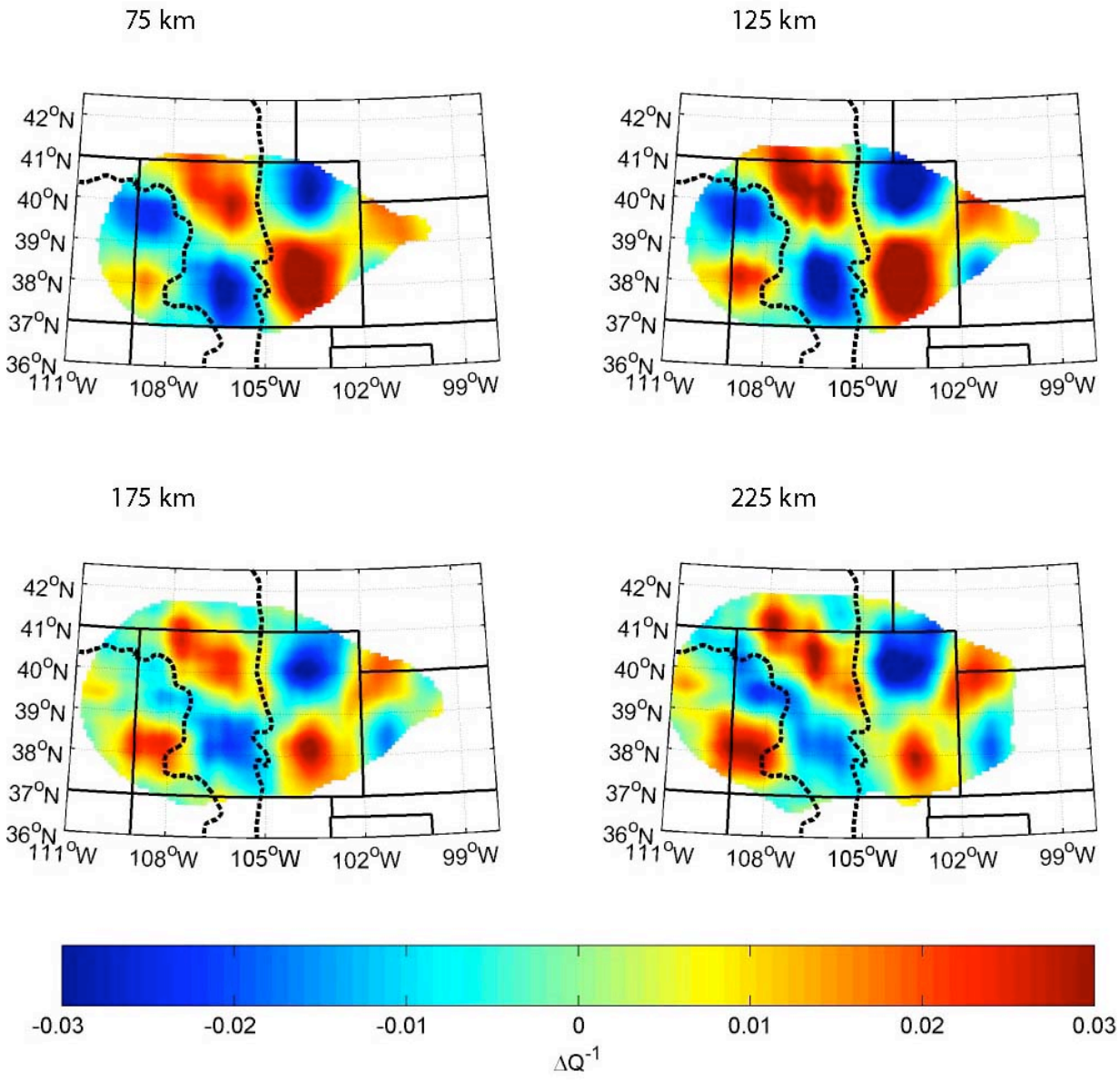

Figure A2.3. Checkerboard results for observations t^* with random error that is 75% of the data variance at four depths. The resulting variance reduction of the checkerboard t^* data is 10%. Resolution continues to be good though becomes increasingly distorted with depth.

Acknowledgements. We thank Karen Fischer and Steve Grand for thorough reviews that helped to substantially improve this manuscript and Randy Keller for his work as editor. Instruments used in the Rocky Mountain Front study were from the IRIS Passcal instrument pool. This work was supported in part by National Science Foundation grants EAR-9614410 and EAR-0003747.

REFERENCES

Al-Khatib, H.H., and B.J. Mitchell, Upper Mantle Anelasticity and Tectonic Evolution of the Western United-States from Surface-Wave Attenuation, *Journal of Geophysical Research*, *96* (B11), 18129-18146, 1991.

Allen, R.M., G. Nolet, W.J. Morgan, K. Vogfjord, B.H. Bergsson, P. Erlendsson, G.R. Foulger, S. Jakobsdottir, B.R. Julian, M. Pritchard, S. Ragnarsson, and R. Stefansson, The thin hot plume beneath iceland, *Geophysical Journal International*, *137*, 51-63, 1999.

Anderson, D.L., Anelasticity, in *Theory of the Earth*, pp. 279-302, Blackwell Scientific Publications, Boston, 1989.

Anderson, D.L., and J.W. Given, Absorption Band Q Model for the Earth, *Journal of Geophysical Research*, *87* (B5), 3893-3904, 1982.

Aranovich, L.Y., and R.G. Berman, A new garnet-orthopyroxene thermometer based on reversed Al_2O_3 solubility in FeO-Al_2O_3-SiO_2 orthopyroxene, *American Mineralogist*, *82*, 345-353, 1997.

Bhattacharyya, J., G. Masters, and P. Shearer, Global lateral variations of shear wave attenuation in the upper mantle, *Journal of Geophysical Research*, *101* (B10), 22273-22289, 1996.

Bina, C.R., and G.R. Helffrich, Calculation of elastic properties from thermodynamic equation of state principles, *Annu. Rev. Earth Planet. Sci.*, *20*, 527-552, 1992.

Bromiley, G.D., and A.R. Pawley, The stability of antigorite in the systems MgO-SiO_2-H_2O (MSH) and MgO-Al_2O_3-SiO_2-H_2O (MASH): The effects of Al^{3+} substitution on high-pressure stability, *American Mineralogist*, *88* (1), 99-108, 2003.

Burchfiel, B.C., Tectonostratigraphic map of the Cordilleran Orogen belt: Conterminous United States, in *The Geology of North America*, edited by M.L. Zoback, Geol. Soc. of Amer., Boulder, 1992.

Catchings, R.D., Regional Vp, Vs, Vp/Vs, and Poisson's Ratios across earthquake source zones from Memphis, Tennesee, to St. Louis, Missouri, *Bulletin of the Seismological Society of America*, *89* (6), 1591-1605, 1999.

Christensen, N.I., Poisson's ratio and crustal seismology, *Journal of Geophysical Research*, *101* (B2), 3139-3156, 1996.

Danckwerth, A., and R.C. Newton, Experimental determination of the spinel peridotite to garnet peridotite reaction in the system MgO-Al_2O_3-SiO_2 in the range 900-1000^o C and Al_2O_3 isopleths of enstatite in the spinel field, *Contributions to Mineralogy and Petrology*, *66*, 189-201, 1978.

Decker, E.R., H.P. Heasler, K.L. Buelow, K.H. Baker, and J.S. Hallin, Significance of past and recent heat-flow and radioactivity studies in the Southern Rocky Mountain region, *Geological Society of America Bulletin*, *100*, 1851-1885, 1988.

Duffy, T.S., and D.L. Anderson, Seismic Velocities in Mantle Minerals and the Mineralogy of the Upper Mantle, *Journal of Geophysical Research*, *94* (B2), 1895-1912, 1989.

Dziewonski, A.M., and D.L. Anderson, Preliminary reference Earth model, *Physics of the Earth and Planetary Interiors*, *25*, 297-356, 1981.

Goes, S., R. Govers, and P. Vacher, Shallow mantle temperatures under Europe from P and S wave tomography, *Journal of Geophysical Research*, *105* (B5), 11153-11169, 2000.

Grand, S.P., and D. Helmberger, Upper mantle shear structure of North America, *Geophysical Journal International*, *76*, 399-438, 1984.

Griffin, W.L., S.Y. O'Reilly, and C.G. Ryan, The composition and origin of sub-continental lithospheric mantle, in *Mantle Petrology: Field observations and High Pressure Experimentation: A tribute to Francis R. (Joe) Boyd*, edited by B.O. Mysen, pp. 13-46, The Geochemical Society, Houston, 1999.

Hacker, B.R., G.A. Abers, and S.M. Peacock, Subduction factory 1: Theoretical mineralogy, densities, seismic wave speeds, and H_2O contents, *Journal of Geophysical Research*, *108* (B1), 2029, doi:10.1029/2001JB001127, 2003.

Hammond, W.C., and E.D. Humphreys, Upper mantle seismic wave attenuation: Effects of realistic partial melt distribution, *Journal of Geophysical Research*, *105* (B5), 10987-10999, 2000a.

Hammond, W.C., and E.D. Humphreys, Upper mantle seismic wave velocity: Effects of realistic partial melt geometries, *Journal of Geophysical Research*, *105* (B5), 10975-10986, 2000b.

Hauksson, E., Crustal structure and seismicity distribution adjacent to the Pacific and North America plate boundary in southern California, *Journal of Geophysical Research*, *105* (B6), 13875-13903, 2000.

Hessler, E.K., Upper mantle seismic structure of the Southern Rocky Mountains - Great Plains transition, M.S. thesis, University of Oregon, Eugene, 1997.

Holland, T.J.B., and R. Powell, An internally consistent thermodynamic data set for phases of petrological interest, *Journal of Metamorphic Petrology*, *16*, 309-343, 1998.

Humphreys, E., and K.G. Dueker, Physical state of the western U.S. upper mantle, *Journal of Geophysical Research*, *99* (B5), 9635-9650, 1994.

Jackson, I., Progress in the Experimental Study of Seismic Wave Attenuation, *Annu. Rev. Earth Planet. Sci.*, *21* (1), 375-406, 1993.

Karato, S., Importance of anelasticity in the interpretation of seismic tomography, *Geophysical Research Letters*, *20* (15), 1623-1626, 1993.

Karato, S., and H. Jung, Water, partial melting and the origin of the seismic low velocity and high attenuation zone in the upper mantle, *Earth and Planetary Science Letters*, *157* (3-4), 193-207, 1998.

Karato, S., and H.A. Spetzler, Defect microdynamics in minerals and solid state mechanisms of seismic wave attenuation and velocity dispersion in the mantle, *Reviews of Geophysics*, *28* (4), 399-421, 1990.

Lay, T., and T.C. Wallace, Multiple ScS Attenuation and Travel-Times beneath Western North-America, *Bulletin of the Seismological Society of America*, *78* (6), 2041-2061, 1988.

Lee, D.-K., and S.P. Grand, Upper mantle shear structure beneath the Colorado Rocky Mountains, *Journal of Geophysical Research*, *101* (B10), 22233-22244, 1996.

Lerner-Lam, A.L., A.F. Sheehan, S.P. Grand, E. Humphreys, K.G. Dueker, E. Hessler, H. Guo, D.-K. Lee, and M.K. Savage, Deep Structure Beneath the Southern Rocky Mountains from the Rocky Mountain Front Broadband Seismic Experiment, *Rocky Mountain Geology*, *33* (2), 199-216, 1998.

Li, A., D.W. Forsyth, and K.M. Fischer, Evidence for shallow isostatic compensation of the southern Rocky Mountains from Rayleigh wave tomography, *Geology*, *30* (8), 683-686, 2002.

Ludwig, W.J., J.E. Nafe, and C.L. Drake, Seismic refraction, in *The Sea*, pp. 53-84, Wiley, New York, 1970.

Meju, M.A., Error analysis in linear inversion, in *Geophysical data analysis: Understanding inverse problem theory and practice*, pp. 294, Society for Exploration Geophysicists, Tulsa, 1994.

Menke, W., Singular Value Decomposition and the Natural Generalized Inverse, in *Geophysical Data Analysis: Discrete Inverse Theory*, pp. 119-124, Academic Press, Orlando, 1984.

Minster, J.B., and D.L. Anderson, A model of dislocation-controlled rheology for the mantle, *Philosophical Transactions of the Royal Society of London Series a-Mathematical Physical and Engineering Sciences*, *299* (1449), 319-356, 1981.

Mutschler, F.E., E.E. Larson, and R.M. Bruce, Laramide and younger magmatism in Colorado - new petrologic and tectonic variations on old themes, *Colorado School on Mines Quarterly*, *1*, 1-47, 1987.

Nataf, H.C., and Y. Ricard, An a priori tomographic model of the upper mantle based on geophysical modeling, *Physics of the Earth and Planetary Interiors*, *95*, 101-122, 1996.

Nowick, A.S., and B.S. Berry, *Anelastic Relaxation in Crystalline Solids*, 677 pp., Academic Press, New York, 1972.

Percival, D.B., and A.T. Walden, *Spectral Analysis for Physical Applications: Multitaper and Conventional Univariate Techniques*, Cambridge University Press, Cambridge, 1993.

Prodehl, C., and P.W. Lipman, Crustal structure of the Rocky Mountain region, in *Geophysical framework of the continental United States*, edited by W.D. Mooney, pp. 249-284, Geol. Soc. of Amer., Boulder, 1989.

Reid, F.J.L., J.H. Woodhouse, and H.J.v. Heijst, Upper mantle attenuation and velocity structure from measurements of differential S phases, *Geophysical Journal International*, *145*, 615-630, 2001.

Romanowicz, B., A global tomographic model of shear attenuation in the upper mantle, *Journal of Geophysical Research*, *100*, 12375-12394, 1995.

Roth, E.G., D.A. Wiens, and D.P. Zhao, An empirical relationship between seismic attenuation and velocity anomalies in the upper mantle, *Geophysical Research Letters*, *27* (5), 601-604, 2000.

Sato, H., and M.P. Ryan, Generalized Upper Mantle Thermal Structure, in *Magmatic Systems*, edited by M.P. Ryan, pp. 259-290, Academic Press, New York, 1994.

Sato, K., T. Katsura, and E. Ito, Phase relations of natural phlogopite with and without enstatite up to 8 GPa: implication for mantle metasomatism, *Earth and Planetary Science Letters*, *146*, 511-526, 1997.

Sheehan, A.F., G.A. Abers, C.H. Jones, and A. Lerner-Lam, Crustal thickness variations across the Colorado Rocky Mountains from teleseismic receiver functions, *Journal of Geophysical Research*, *100* (B10), 20391-20404, 1995.

Sheehan, A.F., and S.C. Solomon, Differential Shear Wave Attenuation and Its Lateral Variation in the North Atlantic Region, *Journal of Geophysical Research*, *97* (B11), 15339-15350, 1992.

Slack, P.D., P.M. Davis, W.S. Baldridge, K.H. Olsen, A. Glahn, U. Achauer, and W. Spence, The upper mantle structure of the central Rio Grand rift region from teleseismic P and S wave travel time delays and attenuation, *Journal of Geophysical Research*, *101* (B7), 16003-16023, 1996.

Snelson, C.M., T.J. Henstock, G.R. Keller, K.C. Miller, and A. Lavender, Crustal and uppermost mantle structure along the Deep Probe seismic line, *Rocky Mountain Geology*, *33* (2), 181-198, 1998.

Sobolev, S.B., H. Zeyen, G. Stoll, F. Werling, R. Altherr, and K. Fuchs, Upper mantle temperatures from teleseismic tomography of French Massif Central including effects of composition, mineral reactions, anharmonicity, anelasticity, and partial melt, *Earth and Planetary Science Letters*, *139*, 147-163, 1996.

Stacey, F.D., Thermal parameters of the Earth, in *Physics of the Earth*, pp. 457-460, Brookfield Press, Kenmore, Brisbane, 1992.

Tarantola, A., *Inverse Problem Theory: Methods for Data Fitting and Model Parameter Estimation*, 613 pp., Elsevier Science, New York, 1987.

Wannamaker, P.E., J.B. Hulen, and M.T. Heizler, Early Miocene lamproite from the Colorado Plateau tectonic province, Southeastern Utah, USA, *Journal of Volcanology and Geothermal Research*, *96*, 175-190, 2000.

Warren, L.M., and P.M. Shearer, Investigating the frequency dependence of mantle Q by stacking P and PP spectra, *Journal of Geophysical Research-Solid Earth*, *105* (B11), 25391-25402, 2000.

Oliver S. Boyd and Anne F. Sheehan, Dept. of Geological Sciences, University of Colorado at Boulder, Campus Box 399, 2200 Colorado Ave., Boulder CO 80309-0399 (email: Oliver.Boyd@Colorado.EDU, Anne.Sheehan@Colorado.EDU)